TECHNICAL MEMORANDUM

208

The singular vector structure of the atmospheric general circulation

R. Buizza and T.N. Palmer

Research Department

January 1995

European Centre for Medium-Range Weather Forecasts
Europäisches Zentrum für mittelfristige Wettervorhersage
Centre européen pour les prévisions météorologiques à moyen

ABSTRACT

The local phase-space instability of the atmospheric general circulation is characterized by its (non-modal) singular vectors. The formalism of singular vector analysis is described. The relations between singular vectors, normal modes, adjoint modes, Lyapunov vectors, perturbations produced by the so-called breeding method, and wave pseudomomentum are outlined. Techniques to estimate the dominant part of the singular spectrum using large-dimensional primitive equation models are discussed. These include the use of forward and adjoint tangent propagators with a Lanczos iterative algorithm. Results are described, based firstly on statistics of routine calculations made between December 1992 - August 1993, and secondly on three specific case studies.

Results define three dominant geographical areas of instability in the northern hemisphere: the two regions of storm-track cyclogenesis, and the north-African subtropical jet. Singular vectors can amplify as much as 10-fold over 36 hours, and in winter there are typically at least 35 independent singular vectors which quadruple in amplitude over this timescale. Qualitatively, the distribution of singular vectors can be associated with a simple diagnostic of baroclinic instability from the basic state flow. However, this relationship is not quantitatively reliable, as, for example, the chosen diagnostic takes no account of the horizontal or time varying structure of the basic state flow.

We identify three basic type of singular vector. The most important and most frequent is located in midlatitudes. At initial time, the singular vector is localized in the horizontal, with most amplitude in the lower troposphere. Energy growth can be interpreted qualitatively in terms of wave pseudomomentum propagation into the jet, resulting in peak amplitudes in the upper troposphere at optimization time. During evolution the dominant horizontal wavenumber of the singular vector decreases. Singular vector growth is therefore fundamentally non-modal. Singular vectors localized firstly in the tropical upper troposphere, and secondly with equivalent barotropic structure in the high-latitude troposphere, were also identified.

1. INTRODUCTION

A principal milestone in the development of dynamical meteorology theory was the description of extratropical cyclones in terms of exponentially-growing shape-preserving solutions of the linearized quasi-geostrophic equations (*Charney*, 1947; *Eady*, 1949). The horizontal scale, vertical structure, phase-speed and e-folding time associated with such solutions correspond well with observations of typical midlatitude depressions.

The existence of such unstable modal structures arises from Charney and Eady's (inspired!) choice of basic states to linearize the equations about. In both models, these basic states are stationary solutions of the equations of motion; they describe highly idealized zonally symmetric flows which incorporate the essential (interior or boundary) potential vorticity gradients necessary to support baroclinic instability.

Studies of atmospheric and oceanic instability have been a central component of geophysical fluid dynamics over the following decades (see e.g. *Gill*, 1982; *Pedlosky*, 1987). Inevitably attention has been given to the modal instability of more complex basic states, including those with zonal asymmetries. In some studies, such zonally asymmetric basic states are taken directly from analyses of the real atmosphere (e.g. *Frederiksen*, 1982; *Simmons et al.*, 1983).

However, there are two profound theoretical problems associated with the application of modal instability theory in atmospheric dynamics. The first (which, as highlighted by *Farrell*, 1982, applies to both Eady and Charney problems, as well as to more complex flows) arises because the set of eigenvectors of the linear evolution operator is not complete (see also *Tung*, 1983). As a result, a general initial disturbance cannot be written as linear combinations of the normal modes, but can be expressed as an integral over the so-called continuous spectrum of the linear evolution operator. However, this (Laplace transform) integral is not constrained to evolve exponentially, and over physically-relevant timescales (e.g. associated with the lifetime of an extratropical depression) the disturbance can grow significantly more rapidly than the fastest-growing normal mode solution, and will not evolve with shape-preserving structure.

If the dynamical equations are truncated (in order to be integrated numerically), then the continuous spectrum is approximated by eigenspectrum of a finite dimensional evolution operator. These eigenvectors are generally linearly independent, so that any initial perturbation can be expressed in terms of the truncated operator's normal modes; however, they are not in general orthogonal. As above, over physically-relevant timescales, linear combinations of two or more modal solutions can grow much faster than any individual mode, and the physical structure of arbitrary perturbations is not time invariant.

The second problem in the application of modal theory arises when studying the instability of basic state flows derived from observations. Typically such flows are not themselves stationary solutions of the equations of motion (even when the basic state is itself a time-average of observed flows). In such a situation, exponentially growing normal mode solutions (of either the continuous or finite system) will not exist. A simple expedient might be to apply a fictitious forcing to the equations of motion to render the basic state a stationary solution. However, this expedient cannot be justified rigorously, and moreover its prescription is not unique (*Andrews*, 1984). This problem gives rise to difficulties of a more practical nature. In particular, as discussed in more detail below, it implies that the time mean instability of the general circulation cannot be deduced from the instability of the time-mean flow.

A restriction to analysis of modal solutions is clearly convenient mathematically (essentially removing one degree of freedom from the problem to be solved), but it is not a necessary ingredient of the physical problem being addressed: to determine those structures whose (suitably-defined) amplitudes grow linearly by an amount $\Delta A/A>1$ over a physically-relevant (e.g. synoptic) timescale Δt relative to some prescribed solution of the nonlinear dynamical equations. As described below, a solution of this physical prescription can be formulated mathematically without reference to modal solutions, exponential growth, or time-invariant basic states. Mathematically, the derived structures are known as singular vectors, and their growth over the prescribed time interval are given by the corresponding singular values (see e.g., *Noble and Daniel*, 1977).

In addition to increasing our understanding the phenomenon of extratropical cyclogenesis, singular vector calculations also provide estimates of the predictability of the atmospheric circulation (*Lorenz*, 1965; *Farrell*, 1990; *Molteni and Palmer*, 1993). Essentially the predictability problem is concerned with determining the evolution of the probability distribution of initial errors. If the initial error distribution is isotropic in phase space, evolving to an ellipsoid at some forecast time, then the major axes of the ellipsoid are determined by the dominant singular vectors. Related to this, singular vectors can be used to provide sets of initial perturbations for ensemble forecasts (*Mureau et al.*, 1993; *Palmer et al.*, 1993). This application of singular vector analysis is not discussed in this paper, but will be dealt with in detail elsewhere.

The singular vectors of an operator L are eigenvectors of the product operator L^*L, where "*" denotes the adjoint operation, equivalent to matrix transposition. (The terminology derives from the fact that the number of positive singular values determines the rank of the operator.) In this paper L determines the evolution of small perturbations relative to some chosen (phase-space) time-evolving trajectory of the nonlinear equations. The completeness of the eigenvectors in the continuous case (with compact L), or their orthogonality in the finite case arises if $L^*L=LL^*$ i.e. L is normal (e.g. *Taylor*, 1958).

For relatively low-dimensional systems (e.g. up to about O(1000) degrees of freedom) conventional matrix-based algorithms can be used to find the full singular spectrum (such as in the barotropic-model studies of *Lacarra and Talagrand* (1988) and *Borges and Hartmann* (1992), or the quasi-geostrophic model of *Molteni and Palmer* (1992)). For more complete multi-level basic state flows e.g. associated with the solution of the primitive equations in numerical weather prediction models, such singular vectors can only be obtained using iterative algorithms (*Buizza et al.*, 1993). In such cases, the adjoint operation must be coded into the FORTRAN statements that describe the evolution operator $\boldsymbol{L}$. At the European Centre for Medium-Range Weather Forecasts (ECMWF), such coding has been done in order to implement a 4-dimensional data assimilation system (*Thépaut and Courtier*, 1991).

In this paper we describe the calculation of singular vectors and singular values from a multi-level primitive equation model using an iterative Lanczos algorithm (*Strang*, 1986). The technique is not restricted to stationary basic states, and the time interval and region over which the amplification $\boldsymbol{\Delta A/A}$ is determined can be specified arbitrarily. In this sense the technique corresponds to one of the most general extensions of the original Charney and Eady instability calculations.

An outline of the paper is as follows. In section 2 we describe the formalism of singular vector analysis. We define the conditions under which the singular vectors reduce either to the normal modes, to their adjoints, to the Lyapunov vectors (e.g. *Parker and Chua*, 1989), or to perturbations obtained by the so-called "breeding" technique (*Toth and Kalnay*, 1993). (Throughout this analysis we deal with a finite dimensional system. In this way, when normal modes exist, we assume that they are complete.) Moreover, to aid interpretation of singular vector structure, we discuss energy amplification in idealized systems where pseudo-momentum (or "wave activity") is conserved (e.g. *Andrews et al.*, 1987; *Held*, 1985). We also describe a general "local projection operator", which enables calculation of singular vector growth, optimized for a specified region of the atmosphere. The numerical implementation of this formalism in the ECMWF Integrated Forecasting System (*Dent*, 1993) is also described in this section.

In section 3 we review some results of singular vector calculations using idealized time-invariant basic state circulations in barotropic and multi-level quasi-geostrophic models.

The implementation at ECMWF of code to calculate the singular spectrum on a routine basis took place in December 1992. In section 4 we analyse some of the principal characteristics of the statistics of these routine calculations over 3 separate seasons. In sections 5 and 6, we study singular vectors from three contrasting basic state flows from the winter of 1992/93; in these cases the dominant singular vector was located over one of the three regions where, from the statistics in section 4, singular vector amplitude at initial time was maximized. In section 5 the analysis is made with global energy optimization; in section 6

we analyze singular vector growth optimized for specific regions around the northern extratropics. Concluding remarks are given in section 7.

2. SINGULAR VECTORS, THEIR RELATIONSHIP WITH OTHER DYNAMICAL QUANTITIES, AND THEIR CALCULATION IN A PRIMITIVE EQUATION NUMERICAL WEATHER PREDICTION MODEL.

2.1 Basic Formalism

We start by writing the ECMWF forecast model in terms of the (finite M-dimensional) nonlinear evolution equation

$$\frac{dx}{dt} = A[x] \tag{2.1}$$

Here the components of the state vector x are the spherical-harmonics expansions of vorticity, ζ, divergence, D, temperature, T, humidity, q, together with the logarithm of surface pressure π (*Simmons et al.*, 1989). The operator A includes not only the nonlinearity of the resolved dynamics, but also nonlinearities in the physical parametrizations.

Consider a small perturbation x' of the state vector x. For sufficiently short time intervals, its evolution can be described by the linearized approximation

$$\frac{dx'}{dt} = A_l x' \tag{2.2}$$

of (2.1). $A_l = \frac{dA}{dx}|_{x(t)}$ is the linear evolution operator evaluated on the nonlinear trajectory $x(t)$.

Equation (2.2) can be written in the integral form

$$x'(t) = L(t,t_0)x'(t_0) \tag{2.3}$$

The operator $L(t,t_0)$ is referred to as the forward tangent propagator; it maps small perturbations along the (nonlinear) trajectory from an initial time t_0 to some future time t. From here on we drop the 'primes' on the perturbation quantities.

We now define an inner product (see also section 2.3)

$$(x;y)=\frac{1}{2}\int_0^1\int_S (\nabla\Delta^{-1}\zeta_x \cdot \nabla\Delta^{-1}\zeta_y + \nabla\Delta^{-1}D_x\cdot\nabla\Delta^{-1}D_y + RT_r\ln\pi_x\ln\pi_y + \frac{C_p}{T_r}T_xT_y)dS\left(\frac{\partial p}{\partial\eta}\right)d\eta \tag{2.4}$$

The quantities ζ_x, D_x ... denote the vorticity, divergence etc components of the state vector x.

In (2.4), C_p, R and T_r are constants, η is the terrain following vertical coordinate used in the ECMWF model and horizontal integration is over the entire globe S. Using (2.3) the perturbation norm at time t is given by

$$\|x(t)\|^2 = (x(t);x(t)) = (x(t_0);L^*Lx(t_0)) \tag{2.5}$$

where L^* is the adjoint of L with respect to the energy inner product, i.e.

$$(x;Ly) = (L^*x;y). \tag{2.6}$$

Unlike L itself, the operator L^*L is normal. Hence its eigenvectors $\mathbf{v}_i(t_0)$ can be chosen to form a complete orthonormal basis in the M-dimensional tangent space of linear perturbations with real eigenvalues $\sigma_i^2 \geq 0$ (e.g. *Noble and Daniel*, 1977) i.e.

$$(L^*L)\mathbf{v}_i(t_0) = \sigma_i^2 \mathbf{v}_i(t_0) \tag{2.7}$$

At future time t, these eigenvectors evolve to $\mathbf{v}_i(t) = L\mathbf{v}_i(t_0)$ which in turn satisfy the eigenvector equation

$$(LL^*)\mathbf{v}_i(t) = \sigma_i^2 \mathbf{v}_i(t) \tag{2.8}$$

From eqs. (2.5) and (2.8),

$$\|\mathbf{v}_i(t)\|^2 = \left(\mathbf{v}_i(t_0);L^*L\mathbf{v}_i(t_0)\right) = \sigma_i^2 \tag{2.9}$$

Since any $x(t)/\|x(t_0)\|$ can be written as a linear combination of the set $\mathbf{v}_i(t)$, it follows that

$$\max_{x(t_0)\neq 0}(\|x(t)\|/\|x(t_0)\|) = \sigma_1 \tag{2.10}$$

The σ_i, ranked in terms of magnitude, are called the singular values of the operator L, and the vectors $\mathbf{v}_i(t)$ are called the singular vectors of L. Maximum energy growth over the time interval $t-t_0$ is therefore associated with the dominant singular vector: $\mathbf{v}_1(t_0)$ at initial time, and $\mathbf{v}_1(t)$ at optimization time.

2.2 Relationship to normal modes, adjoint modes, Lyapunov vectors, the "breeding method", and pseudomomentum conservation

We introduced the notion of singular vector analysis as a generalization of classical normal mode instability analysis. This can be made explicit by linearizing about a stationary solution, so that the operator A_l does not depend on time. Normalized eigenvectors ξ_i of A_l with eigenvalues μ_i give rise to modal solutions $\xi_i e^{\mu_i(t-t_0)}$ of (2.2). The integral operator $L(t,t_0)$ can be written as $\exp[(t-t_0)A_l]$, with eigenvectors ξ_i and eigenvalues $e^{(t-t_0)\mu_i}$.

In general the linear evolution operators associated with realistic stationary basic state flows are generally non normal (with energy inner product) because of vertical and horizontal wind shear (e.g. *Farrell and Moore*, 1992). Because of this, the normal modes are not generally orthogonal to one another. However, irrespective of normality, normalized eigenvectors η_i and eigenvalues θ_i of the adjoint operator L^* must, from (2.6), satisfy the biorthogonality condition

$$(\mu_i-\theta_i^{cc})<\eta_i,\xi_i>=0 \tag{2.11}$$

where "cc" denotes complex conjugate. This condition ensures that the eigenvalues of an eigenvector/adjoint eigenvector pair that are not orthogonal, must form a complex conjugate pair. The magnitude of the inner product $<\eta_i,\xi_i>$ for such eigenvector pairs depends on the angle, α_i, they subtend in phase space. *Zhang* (1988) refers to the factor $1/\cos(\alpha_i)$ as the "projectibility" of ξ_i.

We can generally take the normal modes to be complete in our finite dimensional system so that any initial disturbance can be written as a linear combination of the ξ_i i.e.

$$x(t)=\sum_i c_i\xi_i e^{\mu_i(t-t_0)} \tag{2.12}$$

and from the biorthogonality condition (2.11)

$$c_i=<\eta_i,x(t_0)>/<\eta_i,\xi_i> \tag{2.13}$$

From (2.12), the fastest growing normal mode will ultimately dominate the linear combination. Hence for sufficiently long optimization times, the dominant singular vector at optimization time will correspond to the most unstable normal mode.

In order to maximize the contribution of the first normal mode at optimization time, c_1 in (2.12) should be as large as possible. If $x(t_0)$ equals ξ_1 then $c_1=1$ which could be highly sub-optimal. If fact, if $x(t_0)$ projects onto η_1, then c_1 is maximized and is given by the projectibility factor $1/(\cos\alpha_1)$ (*Zhang*, 1988).

Hence, at initial time, the dominant singular vector will be determined by the first adjoint eigenvector, whilst at (indefinitely long) optimization time the dominant singular vector is determined by the first normal mode itself. This is illustrated schematically in Fig. 1 for an idealized 2-D system with decaying normal modes. The singular value will depend on both the e-folding time of the dominant normal mode and its projectibility. For finite optimization time the dominant singular vectors will no longer project onto individual normal mode solutions (and their adjoints), and the amplitude of finite-time instabilities need not be bounded by properties of the dominant normal modes alone. (It should be noted that, since the eigenvalues are complex whilst the singular values are real, there is some choice as to which phase of the

adjoint mode the initial singular vector should be aligned with. This choice does not affect the amplitude growth of the singular vector.)

If, instead of linearizing about a single stationary point on the climate attractor, we consider the other extreme of linearizing about a (time-evolving) trajectory portion which is sufficiently long to approximately cover the entire attractor, then the singular values again have exponential dependence $e^{\lambda_i(t-t_0)}$ on optimization time. In this limit, the λ_i do not themselves depend on position on the attractor, and are referred to as the Lyapunov exponents (see e.g. *Parker and Chua*, 1989). The corresponding set of singular vectors $\mathbf{v}_i(t)$ can be referred to as the Lyapunov vectors. Note that although the Lyapunov exponents are themselves global quantities, the Lyapunov vectors are still defined locally, and thus vary with position on the attractor, and hence with time.

The correspondence between Lyapunov and singular vectors is important in understanding the relationship between singular vectors and perturbations created by the so-called "breeding" technique (*Toth and Kalnay*, 1993). This technique was introduced as a means to initialise ensemble forecasts (at the National Meteorological Center, Washington), without using adjoint equations. In Toth and Kalnay, a sequence of twin integrations of a full nonlinear weather prediction model are made. Each integration is of length δt. Each pair of integrations comprises a "control", corresponding to the normal "first-guess" forecast used for data assimilation, and a second forecast with initial conditions that differ from the control analysis by a small perturbation. At the end of each integration period, the difference between control and perturbed integrations is rescaled by the initial perturbation amplitude for use in perturbing the initial conditions of the next control integration. This rescaling effectively linearizes perturbation growth at least for meteorologically-relevant scales. Each integration pair can therefore be thought of as defining the propagation operator $L^{TK}(t_m,t_{m-1})$ acting on the difference field. Toth and Kalnay start the sequence with a random initial perturbation $x^{TK}(t_0)$. In the breeding technique, this perturbation develops through operation by the sequence

$$L^{TK}(t_n,t_{n-1})L^{TK}(t_{n-1},t_{n-2}),\ldots,L^{TK}(t_1,t_0) \tag{2.14}$$

where $t_m-t_{m-1}=\delta t$ $(n\leq m\leq 1)$. Strictly speaking, in (2.14) the basic state trajectory is not continuous since at the end of every assimilation cycle, an analysis increment is added to the first guess field. This will not fundamentally change the nature of the calculation.

Acted on by a sufficiently long sequence (2.14), an initial random perturbation will converge to the dominant Lyapunov vector (*Toth and Kalnay*, 1993) in much the same way as a random intial perturbation would converge to the dominant eigenvector in the stationary case, using the power method (see below).

As mentioned above, the dominant Lyapunov vector varies with position on the climate attractor; hence a perturbation produced by the breeding method will evolve from day to day. However, on any given day, the growth of this dominant Lyapunov vector over some specified finite time interval (e.g. the interval δt) will be smaller than the growth of the dominant singular vector optimized for that same time interval since

$$\frac{\|L(t_n,t_{n-1})x^{TK}(t_{n-1})\|}{\|x^{TK}(t_{n-1})\|} \leq \max_{x(t_{n-1})\neq 0} \frac{\|L(t_n,t_{n-1})x(t_{n-1})\|}{\|x(t_{n-1})\|} \tag{2.15}$$

where

$$x^{TK}(t_{n-1}) = L^{TK}(t_{n-1},t_{n-2})....L^{TK}(t_1,t_0)x^{TK}(t_0) \tag{2.16}$$

For example, for the stationary case, $x^{TK}(t_{n-1})$ converges to the dominant normal mode, whilst $x(t_{n-1})$ on the right hand side of (2.15), in the limit of long δt, converges to the adjoint of the normal mode. The right and left hand sides of (2.15) then differ by the projectibility of the dominant normal mode. As shown by *Zhang* (1988), this factor can be as large as 20 for time-averaged wintertime barotropic flows. In some sense, the sub-optimality of the breeding perturbation as a local phase-space measure of growth is inevitable, as it has been calculated without use of the adjoint equations. (Of course, this does not necessarily diminish its importance as a technique for generating initial perturbations for ensemble prediction.)

Whilst it is useful to be able to relate theoretically the general notion of singular vector growth with normal mode and Lyapunov vector analysis, from a practical point of view, for reasons already discussed, these relationships are of limited value in the physical interpretation of singular vector structure and growth from realistic basic state flows. We therefore seek an alternative concept as an interpretive tool for the general results presented in sections 3-6. As such, consider the Eliassen-Palm theorem (*Andrews et al.*, 1987)

$$\frac{\partial}{\partial t}\left(\frac{\overline{q^2}}{2\bar{q}_y}\right) + \nabla.F = 0 \tag{2.17}$$

for small amplitude conservative quasi-geostrophic perturbations of a zonally-symmetric flow $\bar{u}$ with meridional potential vorticity gradient $\bar{q}_y$. (The 'overbar' denotes a zonal average.) The divergence of the Eliassen-Palm vector F is equal to the meridional flux of eddy potential vorticity.

Under WKBJ conditions (ie assuming a slowly varying basic state) it can be shown that (e.g. *Palmer*, 1982)

$$F = \frac{\overline{q^2}}{2\bar{q}_y} c_g \tag{2.18}$$

where c_g is the perturbation group velocity. Equation (2.17) is often referred to as the conservation equation for (wave) pseudo-momentum or wave-activity. Its existence derives from the longitudinal

symmetry of the basic state. In order to analyze this conservation law from an energy point of view, we can derive the equivalent wave-action conservation equation (*Bretherton and Garrett*, 1968)

$$\frac{\partial}{\partial t}\left(\frac{E}{\omega - k\bar{u}}\right)+\nabla.\left(\frac{c_g E}{\omega - k\bar{u}}\right)=0 \tag{2.19}$$

for small amplitude wave packets with local zonal wavenumber k and frequency ω. From (2.19), propagation of pseudomomentum to a region of increasing intrinsic frequency ($\omega - k\bar{u}$) will be associated with an increase in wave energy E.

Fig. 2 (from *Zeng*, 1983) shows the evolution of a dominant trough or ridge line associated with a pseudo-momentum conserving Rossby wavepacket propagating on an idealized zonally symmetric westerly jet (Fig. 2a). Fig. 2b illustrates an energetically-developing barotropic wavepacket, Fig. 2c an energetically-developing baroclinic wavepacket. The phase lines are shown at two different times. The group velocity, shown by double-shafted arrows, points normally to the phase line axis. The zonal phase speed is shown by single-shafted arrows. At the earlier time, both developing solutions have phase surfaces tilted such that the group velocity is focused towards the jet core. The propagation of the wavepacket into the jet leads to a decrease in the tilt of the dominant trough or ridge line at the later time. By (2.19), the focusing of pseudomomentum into the jet leads to an increase in intrinsic frequency and therefore to energy growth (see also, for example, *Orr*, 1907; *Tung*, 1983; *Shepherd*, 1987 for discussion of this type of process).

As will be shown, the structure of many of the computed singular vectors appears to be linked with this process. This appears to be a useful approximation to the full primitive equation calculation because many of the individual singular vectors are strongly localized (compared with their normal mode counterparts). As such, it is possible to approximate their development as if they were propagating on a locally zonally symmetric flow. Of course, as noted above, this approximation must be treated with caution; if the basic state has asymmetries with the same scale as the perturbations, singular vector evolution cannot be approximated by such a solution; we give examples of this below.

2.3 Choice of inner product

In section 2.1 it was stated that calculations in this paper have been made with an energy-based inner product. Another choice might have been the enstrophy inner product

$$\langle x;z\rangle = \int_0^1\int_S q_x\, q_z\, dS \left(\frac{\partial p}{\partial y}\right)dy \tag{2.20}$$

where q_x and q_z denote perturbation potential vorticity, and <..;..> is the canonical L^2 inner product. Yet another choice (at least for zonally-symmetric basic state flows) might be the conserved pseudo-momentum

inner product (*Held*, 1985)

$$\langle x;z\rangle^{p} = \left\langle x;\frac{1}{2\bar{q}_y}z\right\rangle \tag{2.21}$$

where $\bar{q}_y$ is the meridional gradient of the basic state potential vorticity.

The choice of an energy inner product was motivated by the application of this technique to the study of predictability of weather. Maximizing a quadratic quantity based on winds and temperatures is clearly directly relevant to the practice of weather prediction. However, there is another more subtle reason for preferring an energy inner product to, say, an enstrophy inner product. As will be shown below, there is typically an upscale energy cascade between a singular vector at initial time and optimization time (from sub-synoptic to synoptic scale) using the energy inner product. By contrast, initial singular vectors produced with an enstrophy inner product tend to be dominated by planetary-scale perturbations; large scale perturbations have a relatively small enstrophy to energy ratio. During evolution enstrophy generation is maximized by downscale cascade to synoptic scales between initial and optimization time (F. Molteni, personal communication).

In the idealized situation where the atmospheric circulation is measured at the nodes of a uniform grid, measurement error is dominated by its sub grid scale components. The energy inner product is therefore more relevant to describing error growth than the enstrophy inner product. In practice, this idealized situation is not entirely realistic, though it could be argued that operational analyses produce relatively accurate estimates of the planetary scale flow, though relatively poor estimates of the sub-synoptic scale flow.

For zonally symmetric flows, conservation of $\langle x;x\rangle^{p}$ implies from (2.5) that $L^{*p}L = LL^{*p} = I$ where L^{*p} is the adjoint with respect to the pseudomomentum inner product and I is the identity. In this degenerate situation, all the singular values are equal to unity, and hence any orthonormal basis including the basis formed by the orthogonal normal modes can be chosen to form the set of singular vectors.

Whilst the singular vector problem is trivial and degenerate in a space with conserved norm, the complete solution to the physical problem then requires explicit specification of the transform between the inner product space with conserved norm and the inner product space that relates more directly to primary variables such as velocity or vorticity. For example, a perturbation with zero conserved pseudomomentum could, on transformation to the energy or enstrophy norm, be found to be associated with an unbounded exponentially growing instability (*Charney and Stern*, 1962).

In general, however, there are no conserved norms for the perturbations considered in sections 3-5 (since the basic states have no symmetries), and degeneracy of the form discussed above does not appear to arise.

2.4 The Local Projection Operator

The energy inner product (2.4) is defined through integration of perturbation quantities over the whole atmosphere. As such the optimal perturbations are defined to maximise global energy. On the other hand, it is of considerable practical and theoretical interest to be able to identify perturbations whose energy is maximised over a specified region of the atmosphere. This can be achieved by defining a so-called local projection operator. An operator of this type has been studied in a barotropic model by *Barkmeijer* (1992). The operator can also be used to study perturbation growth in local regions of spectral space.

As mentioned above, the components of the state $x(t)$ are largely defined in spectral space. Let S_p represent the spectral-to-grid-point transform, and define a "hat" function

$$g(p) = 1 \quad if \quad p \in \Sigma \tag{2.22a}$$

$$g(p) = 0 \quad if \quad p \notin \Sigma \tag{2.22b}$$

where p is a point and Σ is a specified local region in physical space. Denote by Gx_G the multiplication of a vector x_G, defined in physical space, by the hat function. The local projection operator T is defined as

$$T = S_p^{-1} G S_p \tag{2.23}$$

Since G is diagonal, it is symmetric. Also it is easy to show that S_p is orthogonal, i.e. $S_p^{-1} = S_p^*$. Hence T is self-adjoint, and perturbations chosen for growth inside Σ have norm

$$\|x(t)\|_\Sigma^2 = (Tx(t); Tx(t)) = (x(t_o);\ L^* T^2 L x(t_o)) \tag{2.24}$$

and can be computed from the singular vectors of TL with the (global) energy inner product. It should be noted that the projection operator only acts on perturbations at the final time t; as such there is no constraint that the initial perturbation must be localised within the target area.

The singular values of this operator give the amplification, within the target region, of perturbations with initial unit amplitude in the global energy norm. As with global singular vectors, perturbations produced using the local projection operator are orthogonal in the global sense.

2.5 Numerical Solution of the Singular Value Problem

When systems with a large number of degrees of freedom are considered, the eigenvalue problem (2.7, 2.8) cannot be solved using conventional matrix algorithms. However, iterative techniques provide an alternative

possibility if the adjoint propagator has been coded. The power method, whereby a random initial vector is operated on repeatedly by L^*L, is an example (used to calculate the dominant singular vector in a limited area model by *Vukicevic*, 1991).

A more sophisticated technique is required if more than the largest singular vector is required. The Lanczos algorithm (*Strang*, 1986) is such a technique. As with the power method, a random initial vector is repeatedly operated on by L^*L, but this time the (N<<M) iterates are used to construct an orthonormal (Krylov) basis p_i of an N-dimensional subspace which satisfies the recurrence relationship

$$L^{*E}Lp_j = \beta_{j-1}p_{j-1} + \alpha_j p_j + \beta_j p_{j+1} \tag{2.25}$$

The coefficients α_j, β_j can be determined from this recurrence relationship (and its contraction with p^*_j). If the p_j are taken as columns of an orthogonal matrix P, then from (2.25)

$$W = P^*L^{*E}LP \tag{2.26}$$

is a symmetric tridiagonal matrix. The eigenvectors of W give an approximation of the dominant singular vectors of L.

In practice, we solve a linearized equation in which (2.2) is not the precise linearization of (2.1). In particular, whilst the adiabatic dynamics are precisely linearized, tendencies from the physical parametrizations are not. In fact the only physical parametrization scheme used in the linearized calculations is a simplified boundary layer scheme. This includes a surface drag and vertical diffusion scheme, described in *Buizza* (1994). (It was found necessary to include these processes to suppress fast growing but extremely shallow singular vectors near the surface. These perturbations were deemed meteorologically spurious since they were strongly damped when integrated with the full ECMWF forecast model; *Buizza et al.*, 1993.) Moreover, no humidity components are carried in the tangent models. We note here that it is critical to the success of the calculation that L^* is the precise numerical adjoint of L. In general, we are able to calculate about N/3 singular vectors with acceptable accuracy from N iterations. Results from sections 4-6 have been made with N=100.

The propagator L is itself compounded from the individual operators L_{NNMI}, L_{dyn}, L_{phys}. These denote, respectively, the action of the Non Linear Normal Mode Initialisation (NNMI) procedure (see *Buizza et al.*, 1993), and, for each time step, the action of the adiabatic part of the model equations and of the physical parametrization processes. More precisely, $L(t_N, t_0)$ on an initial state $x(t_0)$ in (2.3) can be decomposed as

$$\left(\prod_{n-1}^{n-N} L_{phys}(t_n, t_{n-1}) L_{dyn}(t_n, t_{n-1})\right) L_{NNMI}(t_0) x(t_0) \tag{2.27}$$

where $t_n - t_{n-1} = \delta t$, the model time step (unrelated to the time interval for the breeding scheme). Similarly the application of the adjoint operator $L^*(t_0, t_N)$ to the vector $x(t_N)$ is given by

$$L^*_{NNMI}(t_0)\left(\prod_{n=N}^{n-1} L^*_{dyn}(t_{n-1}, t_n) L^*_{phys}(t_{n-1}, t_n)\right) x(t_N) \tag{2.28}$$

Here, the adjoint operator is coded with respect to the Euclidean inner product. In all the results shown in sections 4-6 of this paper, a T21L19 truncation of the continuous equations are applied.

The full nonlinear forecast model, the forward and adjoint tangent models, and the Lanczos algorithm, used for the calculations in sections 4-6 of this paper, are components of the ECMWF Integrated Forecast System developed in collaboration with Météo-France (*Courtier et al.*, 1991).

3. STATISTICS OF ATMOSPHERIC SINGULAR VECTORS

In this section we describe the instability characteristics of the climate attractor educed from routine singular vector calculations (three consecutive days per week) made as part of the ECMWF ensemble forecast system. The singular vectors were computed from 100 iterations of the Lanczos algorithm based on a 36 hour optimization time. (For typical initial analysis errors and typical growth rates the linear assumption will break down at about 3 days. Between this time, and about 12 hours, experimentation has indicated that the precise choice of optimization time is not fundamental; *Buizza et al.*, 1993. Our choice for these routine calculations was based on technical expediency.) In this section, we describe an analysis of the statistics of these archived singular vectors and singular values.

Fig. 3a-c shows time series of a selection (1st, 5th and 10th) of singular values for three periods: 19 December - 19 March ("winter"), 20 March - 18 June ("spring") , 19 June - 17 September ("summer"). The vertically-oriented arrows in Fig. 3a are marked against the dates of 3 specific case studies described in sections 5-6. The drop in singular values between the end of the winter and beginning of spring periods is associated with the introduction of the local projection operator (with Σ as the northern hemisphere north of 30N) at this time. (This was done to avoid including as perturbations for the ensemble forecast system, singular vectors e.g. from the southern hemisphere which had little impact on ensemble dispersion over Europe in the early medium range. As mentioned in section 2c, the singular values give the ratio of the perturbation amplitude within the target area at optimization time, to the initial global amplitude. Hence application of the local projection operator inevitably leads to smaller singular values compared with the equivalent global calculation.)

Apart from this sudden drop, the time variation of the singular vectors clearly shows evidence of the seasonal cycle, with largest growth rates in winter, smallest in summer. Moreover, intraseasonal variations

in singular values are also largest in winter and smallest in summer. This accords (respectively) with seasonal dependence on atmospheric high and low-pass transient variability of the northern extratropics.

In general, it can be seen that there is little case-to-case correlation between the time series for the selected singular values (except for exceptional periods such as around 13 February when all singular values were relatively large). This indicates that in general, the chosen singular values are associated with distinct patterns of instability. This contrasts with time series of 1st and 2nd singular values, and to a lesser extent 3rd and 4th singular values, which were strongly correlated (not shown). Such correlations generally signal the existence of local structures in phase quadrature.

In winter, the dominant singular value σ_1 (maximum amplification factor over 36 hours) varies from about 6 to about 10. This corresponding to an initial amplitude doubling time $36/(\sigma_1-1)$ hours of between 7 and 4 hours based on linear growth rates. By contrast the 10th singular value is much less variable, around 5.5. Although the 10th singular values do not have strong intraseasonal variability, it should not be concluded that the spatial structure of the higher-order singular vector also has little case-to-case variability (see below).

Fig. 4 shows the mean singular spectrum for the first 35 singular values averaged over the winter, spring and summer cases. (Beyond the 35th singular value, the Lanczos algorithm, based on 100 iterations, was not deemed sufficiently accurate.) It can be seen that the spectra do not decay strongly with increasing singular value index. For example, in winter, the 35th singular value is equal to about 4 (an equivalent initial amplitude doubling time of about 12 hours). This can be compared with the growth of current forecast errors which typically double in amplitude in about 36 hours. This has implications for assessing the desirable size of an ensemble forecast which will be discussed in a forthcoming paper. Even for the summer season (and with singular vectors optimized for the northern extratropics), the 35th singular vector doubles in amplitude in about 36 hours.

Fig. 5 shows the distribution of the first 5 singular vectors (at initial time) for every case within each of the three seasons. Each square in this figure shows the location of vorticity maximum (at whatever vertical level this occurs) of one such singular vector.

For the winter grouping (Fig. 5a), it can be seen that the amplitude maxima are not distributed homogeneously. Rather they tend to occur in three principal areas in the northern hemisphere: the east Asian/west Pacific region, the northeast American/west Atlantic region, and the northern subtropical African region. The tropics and southern hemisphere extratropics also appear in the northern winter statistics though to a lesser extent. For the spring period (with northern extratropical local projection operator applied), the east Asian/west Pacific region is further accentuated as an area of instability, whilst there are fewer singular

vectors in the northeast American/west Atlantic region. Finally, for the summer period, the singular vectors are more uniformly distributed around the extratropical northern hemisphere than for either of the two previous seasons.

In order to be able to relate these distributions of singular vectors to the underlying basic state flow, we show in Fig. 6 the 'Eady index'

$$\sigma_E \approx 0.31 \frac{f}{N} \frac{du}{dz} \tag{3.1}$$

which is an expression for the growth rate of the most unstable Eady mode (see, for example, *Hoskins and Valdes*, 1990). In (3.1) the static stability N and vertical wind shear du/dz have been estimated using 300 and 1000 hPa potential temperature and wind data from ECMWF archives. Here u denotes the magnitude of the vector wind.

Fig. 6 shows this index for winter, spring and summer, based on 3-month time-mean statistics of wind shear and static stability. Fig. 6a, for winter (December 1 1992 - February 28 1993) shows three principal regions where the Eady index is relatively large: over the western Pacific, over the north Atlantic, and over the middle east. These areas of local maxima are positioned just downstream of the three regions (Fig. 5a), where the wintertime singular vectors are most populous. Fig. 6b, for spring (March 1 1993- 31 May 1993), indicates that the Eady index for the Atlantic is much weaker than for the East Asian/west Pacific region, or indeed for the subtropical African region. As noted above, this is consistent with the distribution of the spring singular vectors (Fig. 5b) for which the Atlantic sector is relatively unpopulated. Finally, Fig. 6c, for summer, shows that the Eady index is much more longitudinally symmetric than for either previous season. Clearly this is related to the relative weakness of the planetary waves in summer. Again, we noted above that the distribution of dominant singular vectors (Fig. 5c) was most zonally uniform in summer.

In a broad sense, therefore, the Eady index is a qualitative diagnostic of the principal regions where singular vectors are located at different times of year. Clearly, the index is not specific to modal growth; its strong dependence on upper tropospheric jet strength makes it a simple measure of both barotropic and baroclinic energy growth. On the other hand, with maximum growth rates of about 1/day, implying amplification factors of about 4.5 over 36 hours, the index (based on seasonal-mean circulation characteristics) underestimates the seasonal-mean growth of almost all the calculated singular vectors.

Returning to winter, the east Asian/west Pacific and northeast American/west Atlantic regions are well known as areas of midlatitude cyclogenesis, as exemplified by climatological maps of (high-pass) transient variance. In contrast, the subtropical African region is not generally thought of as a region of particularly

strong instability, in so far as it is not associated with high climatological transient variability (although desert depressions crossing north Africa have been documented in the literature; *Pedgley*, 1972).

One might postulate two reasons for this. The first is that the singular vector calculations are purely adiabatic. It is possible that in a moist tangent model, the relative importance of the instability of the African jet will be weakened. For example, *Hoskins and Valdes* (1990) have argued that diabatic heating anomalies associated with storm-track activity are necessary to maintain the zone of maximum baroclinity.

However, a second reason is that there is relatively less upstream transience to excite the dominant singular vectors of the African jet. For example, Fig. 7 shows the upper tropospheric jet for the winter 1992/93. Consider the following Gedanken experiment. Imagine a Rossby wave source positioned at the jet entrance (defined by the 30m/s contour) near the west African coast, generating small-amplitude small-scale stochastic transient disturbances propagating downstream and trapped within this mean jet. Imagine also a Rossy-wave sink at the jet exit near Scandinavia. According to the results above, the transient disturbances will be amplified in the three key regions of instability. Since there is a discontinuity in the latitude of the jet maximum over the eastern Atlantic, wave activity from the source region would not be channelled back into the subtropical jet over Africa. As a result, perturbation kinetic energy will be maximized over the two regions of storm track cyclogenesis, rather than in the African jet. This second possibility is consistent with *Farrell and Ioannou's* (1993) speculation that the mean extratropical general circulation should be considered a fairly broadband amplifier of stochastic noise, rather than as an unstable oscillator.

Table 1 gives the initial date for each singular-vector calculation at initial time during the winter period. Against this date is shown the broad location of the dominant singular vector as determined by the position of the initial vorticity maximum. Most of the cases can be categorized according to the three dominant regions: a) over the east Asian/west Pacific region (denoted by "P" in Table 1) b) over the northeast American/west Atlantic region (denoted by "A" in Table 1) and c) over the subtropical African region (denoted by "NA" in Table 1). According to this categorization, the dominant singular vector was positioned most often over the Atlantic region, though during the winter period as a whole, the position of this dominant singular vector varied considerably between the three key winter regions.

We have composited the basic state flow for dates in which the dominant singular vector was positioned in the 3 key regions. For the cases where the dominant singular vector is located in the Atlantic region, there is an enhanced jet over the west Atlantic, consistent with an increase in the Eady index there. For cases where the dominant singular vector is located in the North African region, the composite flow has an anomalous ridge over western Europe, and an anomalous trough over eastern Europe, giving rise to

enhanced flow over north Africa. On the other hand, for cases where the dominant singular vector is located over the Pacific sector, the composite flow does not appear especially anomalous, especially over the west Pacific region itself. We have also studied the variability in the magnitude of the first singular value within each composite; this was largest for the Atlantic singular vector composite, and smallest for the Pacific singular vector composite.

Based on a composite wintertime mean basic state and a 3-level quasi-geostrophic model, *Molteni and Palmer* (1993) concluded that the dominant singular vector of the winter circulation was located over the east Asian/west Pacific region. However, analysis in this paper using time-varying flow supports the conclusion that the dominant singular vector is by no means strongly tied to this particular region. On the other hand, the results suggest that the east Asian/west Pacific region will tend to support the dominant singular vector, unless the flow is particularly anomalous elsewhere. Over the north Atlantic, for the winter 1992/93, the jet over the north Atlantic was anomalously strong, and intraseasonal variability was particularly large (E. Klinker, personal communication).

4. CASE STUDIES OF GLOBAL SINGULAR VECTORS

We choose for individual study, three specific cases during the winter 1992/93, illustrating examples where the dominant singular vector (with global optimization) was positioned either in the Atlantic, Pacific and north African sectors. In order to study developing instabilities over periods closer to the natural timescale set by synoptic-scale disturbances, and yet within the linearity limit of analysis error growth, we have set the optimization time in this section to 3 days. The calculations were made from time-evolving trajectories beginning on 9 January 1993, 8 February 1993 and 6 March 1993 respectively.

From Fig. 3a it can be seen that the first singular value was especially large for the first and third of these dates. The synoptic evolution across the north Atlantic during the period around 9th January included the development of an exceptionally severe depression in the north Atlantic, named the "Braer Storm" because of its unfortunate consequences for the stricken oil tanker "Braer" which ran aground on the Shetland Islands at this time (*Mansfield*, 1993). The period around 6 March 1993 also proved to be exceptionally unsettled over the middle east. This was particularly noticeable from satellite cloud imagery (G. Kelly, personal communication). It is interesting to note that north African desert depressions are most common in the springtime (*Pedgley*, 1972). By contrast singular values for the third period were not exceptional (see Fig. 3a); in some approximate sense this case could be thought of as corresponding to the idealized time-averaged basic-state calculation of *Molteni and Palmer* (1993).

Figs. 8-10 show the streamfunction of the dominant singular vector at initial (left hand panels) and optimization time (right hand panels) for the three chosen dates. They are illustrated on model levels 7, 13

and 15; corresponding approximately to 200, 700 and 850 hPa respectively. Note that at optimization time, the contour interval is 20 times larger than at initial time.

At initial time, the singular vectors have greatest amplitude in the lower model levels, and are spatially localized to the three specific regions of interest. In all three cases there is evidence of barotropic tilt in the trough or ridge lines, particularly at the lower levels, similar to the WKBJ solution in Fig. 2b. Between levels 15 and 13, these trough and ridge lines also show evidence of a westward tilt with height consistent with upward propagation of wave activity. At optimization time, the structure of the singular vectors reflects their upward and downstream propagation, upscale development and energy growth. Downstream propagation is largest for the 9 January case (Fig. 8) associated with the strong zonal winds throughout the depth of the troposphere across the Atlantic (see below). Upscale development can be seen clearly at the lower model levels where the relatively short horizontal wavelength at initial time evolves to a longer wavelength more typical of the upper-tropospheric singular vector perturbations. In all three cases, the final structure has lost most of the energy-amplifying barotropic tilt. On the other hand, the singular vectors exhibit evidence of continued pseudomomentum propagation in the vertical, particularly in the upper troposphere, where amplitude is largest.

The growth in energy apparent in Figs. 8-10 is shown explicitly as a function of model level in Fig. 11a-c. The initial (dashed) energy profile has been multiplied by a factor of 20 in order to show it clearly in relation to the final (solid) energy profile. For the two mid-latitude singular vectors, perturbation energy is largest in the lower model levels at initial time and is largest at the jet level at optimization time. This result is consistent with the WKBJ analysis in section 2. In particular the evolution in the amplitude distribution with height, and the westward phase tilt, can be interpreted in terms of wave activity propagating from a region in the lower troposphere where the intrinsic wave frequency is small, to a region in the upper troposphere where the intrinsic wave frequency is large. From 2.19 this would result in a relatively large growth in energy.

However, of the three cases illustrated, the amplification of energy is largest for 6 March where the dominant singular vector was located over north Africa, and energy was maximized in the lower troposphere. In fact this behaviour was not typical of north African singular vectors; more usually the energy at final time peaked in the upper troposphere, similar to that in Fig. 11a,b. It can be seen from Fig. 3 that the large singular value for 6 March was not repeated on the two following days, despite the fact that the dominant singular vector for 7 and 8 March continued to be located in the north African region (see Table 1). It is possible that the uniquely large singular value for 6 March may have arisen, not only as a result of growth from the locally zonal flow, but also from quasi-resonant interaction between the singular vector perturbation, and similar scale zonal asymmetries in the basic state. Such resonances may be more

likely if downstream singular vector propagation is relatively small; of the 3 cases shown, such propagation was weakest for the 6 March case. Further studies are required to clarify the importance of such a mechanism.

The non-modal character of the singular vectors has been demonstrated through the time evolution of the horizontal and vertical structure. One aspect of this structure, the upscale energy transfer, is shown explicitly in Fig. 12a. This shows, for the 9 January 1993 case, the initial and final energy of the dominant singular vector, as a function of the total (horizontal) wavenumber. As in Fig. 11, the solid line refers to values at optimization time; the dashed line refers to values at initial time multiplied by a factor of 20 to make them visible. It can be seen that at optimization time the energy peaks at about wavenumber 10, well within the range of synoptic scales. By contrast, at initial time the singular vector peaks at a wavenumber close to the truncation limit of the model, and below the range of synoptic scales. Further calculations with a higher resolution (T42) singular vector calculation (Fig 12b) suggest that the initial spectrum is fairly broad at subsynoptic scales, but peaking at about wavenumber 25.

These calculations suggest that the singular vectors, albeit linear, are capable of describing an upscale energy transfer reminiscent of a nonlinear turbulence cascade. Since the basic state is an unapproximated solution of the equations of motion, Rossby triad interactions between the basic state and the perturbation field can generate such upscale evolution. Indeed it could be argued that these singular vector calculations would describe (with a sufficiently high resolution model) the "butterfly effect" in its original (*Lorenz*, 1963) sense, that small scales can influence large scales.

The position of the vorticity maxima of the first 10 singular vectors is shown in Fig. 13 for each of the three cases. These maxima are marked by the index 'i' of the singular value σ_i. In the 9 January and 6 March cases, the first two singular vector maxima are close together, indicative of a propagating phase-quadrature pair. For 8 February, the first and second singular vectors are located in distinct regions (the Pacific and Atlantic respectively). As noted above, this latter situation is unusual. Also, for two of the three cases, there are singular vectors in the tropics and in the southern hemisphere. Indeed, for the 9 January, the 3-9th singular vectors lie outside the northern extratropics. Whilst higher order singular values may not have substantial case-to-case variability (see Fig. 5), Fig. 13 shows that the associated higher-order singular vectors do vary significantly in their physical location.

As discussed above, with 100 iterations, the Lanczos scheme is used to calculate reasonably accurately the first 35 singular vectors and singular values. The spectrum of singular values is shown in Fig. 14 for the three cases. Whilst the first and second dominant singular values are overwhelmingly the largest for the 6 March case, singular values further down the spectrum are generally larger for the 9 January case. We

can compare growth rates for the 72 and 36 hour optimization times by comparing the equivalent exponents $\ln \sigma_1 / \Delta t$. On average, growth rates decrease with increasing optimization time, e.g. for the 9 January and 6 March cases, the exponent equals about 1.5 for 36 hour optimization, and about 1.0 for 72 hour optimization.

In the previous section, we were able to relate some aspects of the statistics of the singular vectors to the basic state flow, using the Eady index (3.1). Here we show the index for the initial dates of the three cases under investigation (Fig. 15). As above, this index is a good qualitative predictor of the regions where dominant singular vectors will be located. For example, over north Africa, the index is clearly largest for 6 March , whilst over the Atlantic it is largest for 9 January. In general it can be seen, comparing Figs. 13 and 15, that there is a region of relatively large Eady index (exceeding 1/day) close to, or just downstream of, an extratropical singular vector maximum. On the other hand, there is no indication in Fig. 15 of why the dominant singular value was so large for the 6 March case; also there are regions of large Eady index with no close singular vector maximum. As mentioned above, one must therefore treat this diagnostic with caution as it only partially describes the envelope of the singular-vector structure of the general circulation.

We conclude this section by noting that not all the higher order singular vectors correspond in structure to the examples illustrated above and cannot be understood in terms of the WKBJ concepts outlined above. For example, the 4th singular vector for the 9 January case is essentially tropical (see Fig. 16a,b). At initial time it describes an essentially north-south dipole disturbance in the upper tropospheric streamfunction over the tropical Atlantic. There is little amplitude in the lower troposphere (see Fig. 12d). At optimization time, the dipole has an east-west orientation in the tropics, again with amplitude concentrated in the upper troposphere (again see Fig. 12d). Over Europe, the perturbation has some amplitude through the depth of the troposphere (and projects onto the singular spectrum with European local projection operator; see section 6). We have replicated the linear evolution of this singular vector in identical-twin integrations of the full diabatic nonlinear ECMWF model, and therefore believe it to be realistic. The 4th singular vector for the 6 March case is also illustrated in Fig. 16. Unlike other extratropical singular vectors shown, the initial structure shows significant amplitude in the upper troposphere, with a zonal perturbation over polar latitudes, and a secondary perturbation over Scandinavia and the north-east Atlantic. These features are relatively large scale, and have an equivalent barotropic structure in the vertical. At optimization time, the dominant region of amplification is over Europe, particularly in the upper troposphere. In all three cases studied we were able to find examples of this type within the first 35 singular vectors.

5. SINGULAR VECTORS USING THE LOCAL PROJECTION OPERATOR

In section 2.4 we described the formalism for estimating the dominant singular vectors with energy growth optimized for a specified region of the atmosphere. Apart from the intrinsic value of being able to study

geographically-localized instability, the technique is of practical value for estimating short-range forecast predictability in specified regions. Local singular vectors for the case studies above have been calculated for local regions between 30N and 60N, and intervals of 30 degrees longitude. We will illustrate some examples of these focusing in particular on the longitude intervals 0-30E, which includes part of Europe. In all the cases described the energy integrals are taken over the entire depth of the atmosphere (though in principle the local projection operator can be applied in the vertical as well as in the horizontal). As in section 5, optimization time is 72 hours.

As examples, Fig. 17 shows the dominant singular vectors, optimized for the region 30-60N, 0-30E for the 9 January and 6 March initial dates. For brevity we only show level 7 and 13 streamfunction at initial time. It can be seen that the basic state flow has a major influence on the location of initial perturbations. For 9 January, there is a maximum in initial amplitude over the north American eastern seaboard, whilst for the 6 March case, the initial amplitude is maximized over Europe, north Africa, and the eastern Atlantic.

This sensitivity of initial pattern to basic state has some obvious practical consequences. For example, a skilful three day forecast for Europe from 9 January will require an accurate wind near the eastern seaboard of north America. On the other hand, a skilful three day forecast for Europe from 6 March requires an accurate in situ analysis. The relatively larger dominant singular value for 9 January (8.5 compared with 7 for 6 March) places particular importance on accurate measurements for the January case.

In Fig. 18 we show the position of the vorticity maxima of the first 10 singular vectors for the 3 cases, and for three chosen areas: the European area above, and the regions 30-60N, 120E-150E and 30-60N, 90-120W. For the European area 9 of the 10 local singular vectors lie upstream of the target region for the 9 January case (the 10th lies in the tropics). By contrast, for the other two cases, the singular vectors lie within or close to the European target region. Comparison of the Eady indices (Fig. 15) close to, and upstream of, the target region, reveals basic-state differences that can account qualitatively for this result. The distribution of the local singular vectors for the other target areas similarly depends on the basic state flow. For example, for the sector including Japan, most singular vectors are located in situ for 9 January (though the dominant singular vector is positioned over the middle east), whilst for the 8 February, most singular vectors are located over central Asia. Similarly, for the North American sector, all the initial singular vectors lie close to Hawaii for 6 March, whilst for other dates, a number of singular vectors are located to the north, e.g. near the Gulf of Alaska. For these regions, the relationship between singular vector location and the in situ and upstream Eady index (Fig. 15), is plausible, though not clear cut.

We have calculated the projection of each of the local singular vectors in Fig. 17 onto each of the global singular vectors, for each of the three chosen dates. For example, the dominant global singular vector for

the 9 January case (Fig. 8) has a correlation of 0.81 with the dominant singular vector computed using the European local projection operator. In the subspace comprising the first 10 global singular vectors, no other singular vector correlates with this dominant local singular vector by more than .04. By contrast the dominant local singular vector for the 6 March does not correspond to a pure global singular vector, but correlates principally with the first second and fourth global singular vectors. As discussed above, the first and second global singular vectors both describe the instability of the subtropical African jet, and form a phase-quadrature pair. The third global singular vector, a Pacific perturbation, has no projection onto the dominant local singular vector. The fourth global singular vector, which at initial time has a strong equivalent barotropic vertical structure over northern Europe, was shown in Fig. 16.

In general, our analysis has suggested that, at least in wintertime, the dominant singular vectors computed using a local projection operator as above, can be reconstructed from the first 35 global singular vectors.

As mentioned in section 2.4, it is also possible to apply the projection operator directly in spectral space. Using this, it has been shown that if the initial and final singular vector for the 9 January case are both constrained to be in the wavenumber 0-10 band, then energy growth is severely reduced (not illustrated). On the other hand, if the initial singular vector is constrained to the wavenumber band 11-20, whilst the final singular vector is constrained to the wavenumber band 0-10, then energy growth is similar to that shown in Fig. 13. Again this confirms the non-modal character of the singular vectors.

7. CONCLUSIONS AND DISCUSSION

We have described a singular-vector formalism for characterizing the growth of linear perturbations over finite times and arbitrary target regions, relative to general (finite dimensional) time-evolving solutions of the nonlinear primitive equations of the atmospheric general circulation. Maximal linear growth is associated with the singular vector with largest singular value. Incorporation of an iterative Lanczos scheme allowed calculation of the first 35 singular vectors to be estimated from the ECMWF Integrated Forecasting System. This system includes the forward and adjoint tangent equations of the full nonlinear forecast model. The technique offers a complete generalization of classical normal-mode instability analysis.

The relationships between singular vectors, normal modes, adjoint modes, Lyapunov vectors, and perturbations created using the breeding method (*Toth and Kalnay*, 1993) have been explored. However, these relationships only hold in rather restrictive conditions (e.g. linearizing about stationary nonlinear solutions, or in the limit of long phase-space trajectory portions). In order to aid further interpretation of singular vector evolution we also described the relationship between energy growth and wave pseudomomentum conservation.

We have described some statistics of the singular vector structure of the atmospheric general circulation, derived from calculations made routinely as part of the operational ECMWF forecast suite. Three preferred regions were identified for significant singular vector growth: the east Asian/west Pacific sector, the northeast United States/ west Atlantic sector, and subtropical north Africa. The first two of these are familiar regions of cyclogenesis, and correspond to areas in which high pass transient variances are maximized. The subtropical region is not distinguished as an area of high transient variability; however, we speculate that, in part, this can be understood from a paradigm of the atmospheric general circulation as a broadband amplifier, rather than an unstable oscillator, and that transient disturbances entering the west Atlantic or west Pacific areas are much larger than those entering the subtropical north African region.

To a first approximation, the distribution of the singular values as a function of time of year was related to the classical Eady measure of baroclinic instability. On the other hand, for a 36 hour optimization period, the growth rates associated with the singular vectors were larger than implied by this diagnostic. For example, for winter, the dominant (synoptic-scale) singular vector increased as much as ten-fold over 36 hours; even the 35th fastest growing singular vector typically increased by a factor of 4.

For the cases studied, the dominant singular vector at initial time had maximum amplitude in the lower troposphere with strong phase-line tilts indicative of energy growth from both barotropic and baroclinic processes. At optimization time, this type of singular vector typically had maximum amplitude in the upper troposphere, with greater horizontal scale. This structure can be partially understood from pseudomomentum conserving wave propagation in a inhomogeneous medium.

We also studied the upscale transfer of energy between initial and final time. In particular, at initial time, energy was dominated by sub synoptic scales (especially when the resolution of the singular vector calculation was increased); on the other hand, at optimization time, the energy was dominated by synoptic scales. This illustrates graphically the butterfly effect in the full sense it was originally intended (*Lorenz*, 1963), i.e. not only small amplitudes, but also small scales could ultimately influence large scales. The spatial transformation of the singular vectors between initial and final time is indicative of their profoundly non-modal structure.

The ability to simulate upscale energy transfer is a consequence of the fact that the basic state is itself an unsmoothed solution of the nonlinear equations. This raises the issue that the instability characteristics of a smooth time-mean atmospheric state will not correspond to the time-mean instability characteristics of the climate attractor. This non-commutativity of time averaging also applies to simpler nonlinear systems than the atmosphere.

In setting up the formalism for calculating linear perturbation growth, we described the ability to find optimal amplification, not only for the globe, but also for a specified region of the atmosphere, using a so-called local projection operator. Some examples showed the dependence of local singular vector structure to basic state.

Although the calculations described in this paper have been made with time-evolving trajectories, the specific cases were not chosen on the basis that the large-scale flow pattern evolved significantly over the optimization period. However, as highlighted in *Palmer* (1993), one of the most potentially useful applications of singular vector analyses both for weather forecasting and climate prediction, is for studies of transient periods in which the atmosphere evolves from one specific weather regime to another.

For such studies, the trajectory length should be sufficiently long to be able to identify such regime transitions. This would appear to suggest optimization periods of around 5 to 7 days, somewhat longer than those we have studied so far, and possibly outside the range in which analysis error growth can be confidently treated as linear. One way of alleviating this problem might be to apply the local projection operator in spectral space to optimize energy growth onto the large synoptic and planetary-scales, where amplitude doubling times are smaller. Indeed since such scales are more directly associated with regime transitions, use of such a projection may be most appropriate in any case for this type of study.

Finally we note that the methodology employed here may also be of use in diagnosing model systematic error. Specifically, it should be noted that in order to have a significant impact on the systematic error of medium range forecasts, errors associated with either physical or numerical processes (or some interaction between the two) should have maximum projection onto the initial singular vector structure, rather than the final structure. Hence, for example, if a model has a tendency to produce excessive eddy kinetic energy near the jet level at the beginning of the medium range, the error may be associated with a systematic misrepresentation of processes near the top of the boundary layer in regions of cyclogenesis, rather than with an in situ systematic error in the upper troposphere. We intend to explore further the use of singular vectors in the diagnosis of model systematic error.

ACKNOWLEDGEMENTS

We acknowledge F. Molteni R. Mureau and J. Tribbia who have contributed to the development of the predictability forecast system at ECMWF both scientifically and technically. We acknowledge the help of E. Klinker in producing the Eady indices shown in the paper. We also thank P. Courtier, A. Hollingsworth and A. Simmons for helpful comments on an early draft of the paper. The Lanczos scheme used here was written by Professor B.N. Parlett, and the code was kindly supplied to us (in pre-release form) by the Numerical Algorithms Group. The comments of three anonymous referees are gratefully acknowledged.

REFERENCES

Andrews, D.G., 1984: On the stability of forced non-zonal flows. Quart.J.Roy.Meteor.Soc., 110, 657-662.

Andrews, D.G., J.R. Holton and C.B. Leovy, 1987: Middle Atmosphere Dynamics. International Geophysics Series. Vol 40, Academic Press. 489pp.

Barkmeijer, J., 1992: Local error growth in a barotropic model, Tellus, 44A, 314-323.

Borges, M.D. and D.L. Hartmann, 1992: Barotropic instability and optimal perturbations of observed non-zonal flows. J.Atmos.Sci., 49, 335-354.

Bretherton, F.P., and C.J.R. Garrett 1968: Wavetrains in inhomogeneous moving media. Proc.Roy.Soc., A302, 529-554.

Buizza, R., J. Tribbia, F. Molteni and T.N. Palmer, 1993: Computation of Optimal Unstable Structures for a Numerical Weather Prediction Model. Tellus A, 45A, 388-407.

Buizza, R., 1994: Sensitivity of optimal unstable structures. Quart.J.Roy.Meteor.Soc., 120, 429-451.

Charney, J.G., 1947: The dynamics of long waves in a baroclinic westerly current. J. Meteor., 4, 135-163.

Charney, J.G. and M.E. Stern, 1962: On the stability of internal baroclinic jets in a rotating atmosphere. J.Atmos.Sci., 19, 159-172.

Courtier, P., C. Freydier, J.-F. Geleyn, F. Rabier and M. Rochas, 1991: The Arpege project at Météo-France. Proceedings of ECMWF Seminar on "Numerical methods in atmospheric models", Shinfield Park, Reading RG2 9AX, U.K., 9-13 September 1991, Vol. 2, 193-231.

Dent, D.W., 1993: Parallelization of the IFS model. In "Parallel supercomputing in atmospheric science" edited by G.R. Hoffmann and T. Kauranne. World Scientific Publishing Co., Singapore. 532pp.

Eady, E.T., 1949: Long waves and cyclone waves. Tellus, 1, 33-52.

Farrell, B.F., 1982: The growth of disturbances in a baroclinic flow. J.Atmos.Sci., 39, 1663-1686.

Farrell, B.F. and A.M. Moore, 1992: An adjoint method for obtaining the most rapidly growing perturbation to oceanic flows. J.Phys.Oceanogr., 22, 338-349.

Farrell, B.F. and P.J. Ioannou, 1993: Stochastic forcing of perturbation variance in unbounded shear and deformation flows. J. Atmos. Sci., 50, 200-211.

Frederiksen, J.S., 1983: Disturbances and eddy fluxes in northern hemisphere flows: instability of three-imensional January and July flows. J.Atmos.Sci., 40, 836-855.

Gill, A.E., 1982: Atmosphere-Ocean Dynamics. International Geophysics Series. Volume 30. Academic Press. 662pp.

Held, I.M., 1985: Pseudomomentum and the orthogonality of modes in shear flows. J.Atmos.Sci., 42, 2280-2288.

Hoskins, B.J., and P.J. Valdes 1990: On the existence of storm-tracks. J.Atmos.Sci., 47, 1854-1864.

Lacarra, J.-F. and O. Talagrand, 1988: Short-range evolution of small perturbations in a barotropic model. Tellus, 17, 321-333.

Lorenz, E N, 1963: The predictability of hydrodynamic flow. Trans. New York Acad. Sci., Ser. 2, 25, 409-432.

Lorenz, 1965: A study of the predictability of a 28-variable atmospheric model. Tellus, 17, 321-333.

Mansfield, D.A., 1993: The storm of 10 January 1993. Met.Mag., 122, 140-146.

Molteni, F. and T.N. Palmer, 1993: Predictability and finite-time instability of the northern winter circulation. Quart.J.Roy.Meteor.Soc., 119, 269-298.

Mureau, R., F. Molteni and T.N. Palmer, 1993: Ensemble prediction using dynamically-conditioned perturbations. Quart.J.Roy.Meteor.Soc., 119, 299-323.

Noble, B. and J.W. Daniel, 1977: Applied Linear Algebra. Prentice-Hall Inc. 477pp.

Orr, W., 1907: Stability of instability of the steady motions of a perfect fluid. Proc.Roy.Irish Acad., pp 9-69.

Palmer, T.N. 1982: Properties of the Eliassen-Palm flux for planetary-scale motions. J.Atmos.Sci., 38, 844-855.

Palmer, T.N., 1993: Extended-range atmospheric prediction and the Lorenz model. Bull.Am.Met.Soc., 74, 49-65.

Palmer, T.N., F. Molteni, R. Mureau, R. Buizza, P. Chapelet and J. Tribbia, 1993: Ensemble prediction. Proceedings of the ECMWF 1992 Seminar.

Parker, T.S. and L.O. Chua, 1989: Practical numerical algorithms for chaotic systems. Springer-Verlag.

Pedlosky, J., 1989: Geophysical Fluid Dynamics. Springer-Verlag. New York, 709pp.

Pedgley, D.E., 1972: Desert depressions over north Africa. Met.Mag., 101, 228-244.

Shepherd, T.G., 1987: Rossby waves and two-dimensional turbulence in a large-scale zonal jet. J.Fluid Mech., 183, 467-509.

Simmons, A.J., J.M. Wallace and G.W. Branstator, 1983: Barotropic wave propagation and instability, and atmospheric teleconnection patterns. J.Atmos.Sci., 40, 1363-1392.

Simmons, A.J., D.M. Burridge, M. Jarraud, C. Girard and W. Wergen, 1989: The ECMWF Medium-Range Predction Models Development of the Numerical Formulations and the Impact of Increased Resolution. Meteorol.Atmos.Phys., 40, 28-60.

Strang, G., 1986: Introduction to applied mathematics. Wellesley-Cambridge press, 758pp.

Taylor, A.E., 1958: Introduction to functional analysis. John Wiley and Sons. New York. 423pp.

Thépaut, J.-N. and P. Courtier, 1991: Four dimensional variational data assimilation using the adjoint of a multilevel primitive equation model. Quart.J.Roy.Meteor.Soc., 117, 1225-1254.

Toth, Z. and E. Kalnay, 1993: Ensemble forecasting at NMC: the generation of perturbations. Bull.Am.Met.Soc., 74, 2317-2330.

Tung, K., 1983: Initial-value problem for Rossby waves in a shear flow with critical level. J.Fluid Mech., 133, 443-469.

Vukicevic, T., 1991: Nonlinear and linear evolution of initial forecast errors. Mon.Wea.Rev., 119, 1602-1611.

Zeng, Q.-C., 1983: The evolution of a Rossby-wave packet in a three dimensional baroclinic atmosphere. J.Atmos.Sci., 40, 73-84.

Zhang, Z., 1988: The linear study of zonally asymmetric barotropic flows. PhD Thesis. University of Reading, UK.

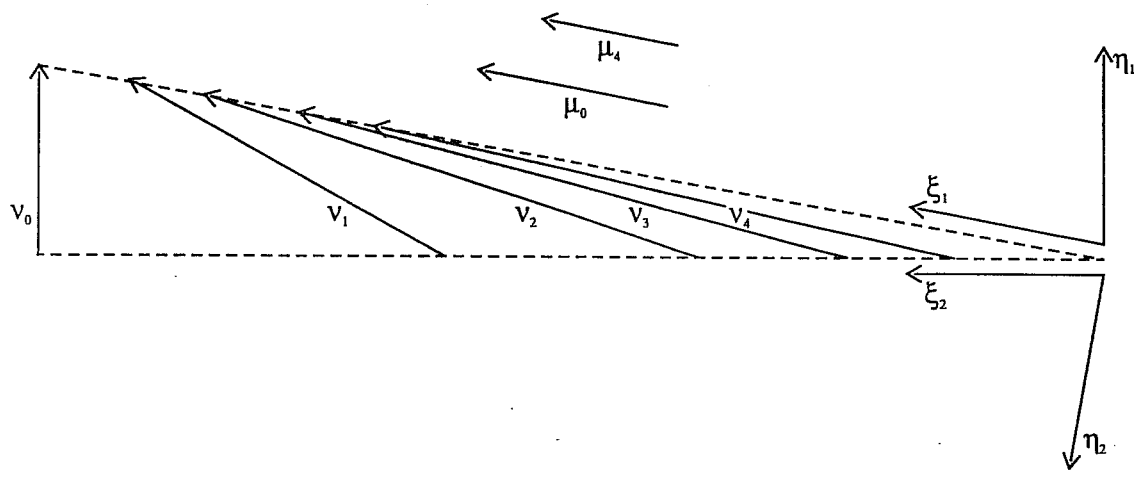

Fig. 1 This diagram illustrates schematically the crucial difference between normal mode and singular vector growth, and the relationship between singular vectors and adjoint modes. An idealized 2-D system has two very non orthogonal decaying modes ξ_1 and ξ_2. We take ξ_1 to have the larger real eigenvalue component. The adjoint modes η_1 and η_2 are shown, with η_1, η_2 orthogonal to ζ_2, ζ_1 respectively (according to the biorthogonality condition 2.11). A normalised vector v_o is shown parallel to η_1. Its time evolution can be estimated by mapping the tip and tail of v_o along the ξ_1 and ξ_2 directions (shown as dashed lines) using the modal decay rates. The sequence of vectors v_n n=1,2 .. giving the time evolution of v_o increases in amplitude up to some finite n=N, and is aligned almost entirely with ξ_1 for large n. The projection of v_n onto ξ_1 for large n is much larger than that associated with the evolution of a second normalized vector μ which is initially aligned along ξ_1. The sequence v_n describes singular vector growth over a long time interval.

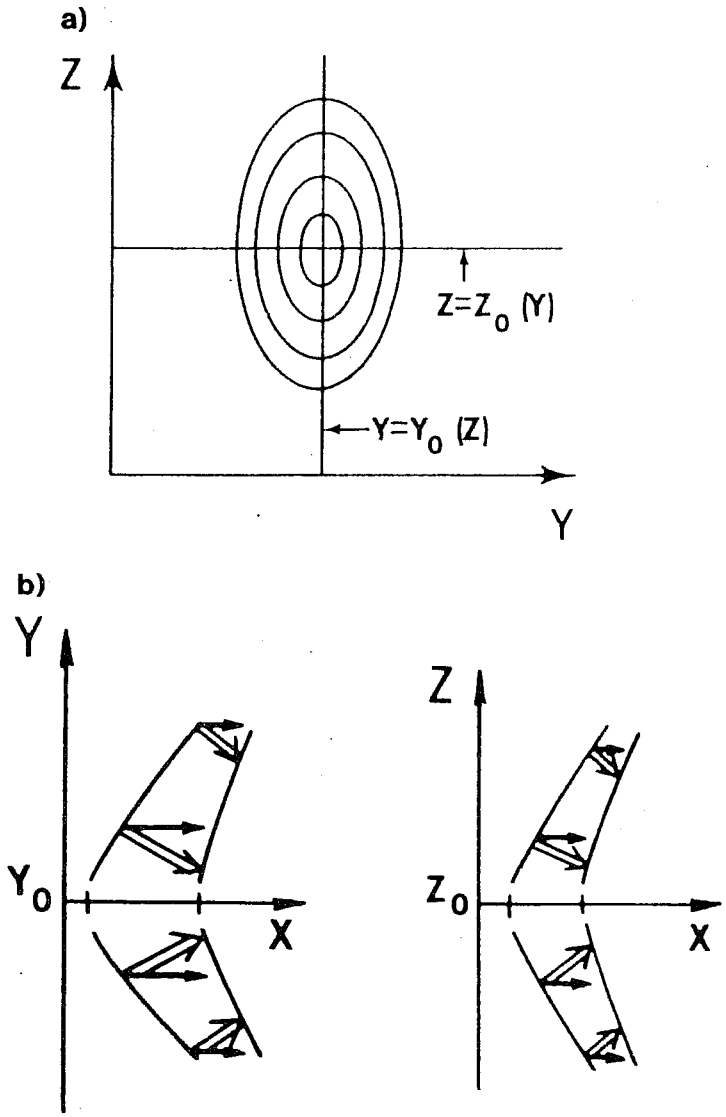

Fig. 2 The evolution of an energetically-amplifying Rossby wavepacket in a linear WKBJ approximation (from *Zeng*, 1983) with conserved pseudo-momentum. a) The basic state comprising an idealized zonally symmetric jet. b) The evolution of a dominant wavepacket ridge or trough line associated with barotropic energy growth. c) The evolution of a dominant wavepacket ridge or trough associated with baroclinic energy growth. The wavepacket group velocity is shown as double arrows, the zonal phase speed as single arrows (From *Zeng*, 1983).

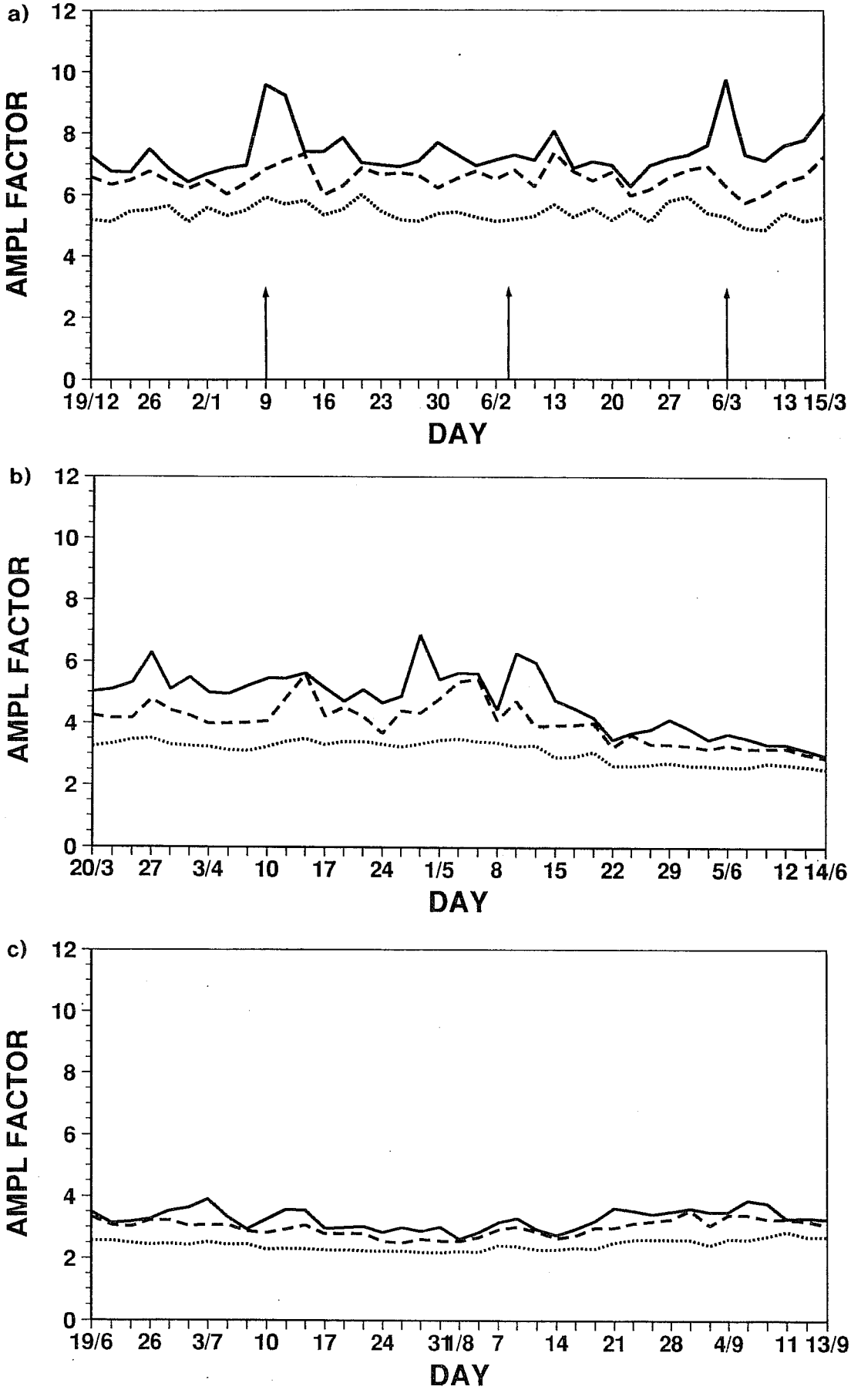

Fig. 3 Time-series of the 1st (solid), 5th (dashed) and 10th (dotted) singular values from operational ECMWF archives for three periods: a) 19 December 1992 - 19 March 1993 ("winter"), b) 20 March 1993 - 18 June 1993 ("spring"), c) 19 June -17 September ("summer"). For the winter period, the singular vectors were calculated with a global optimization. For the spring and summer periods, they were calculated using a local projection operator for the extratropics north of 30N. The dates for 3 specific case studies discussed in sections 5-6 are shown by the vertically-oriented arrows in Fig. 3a.

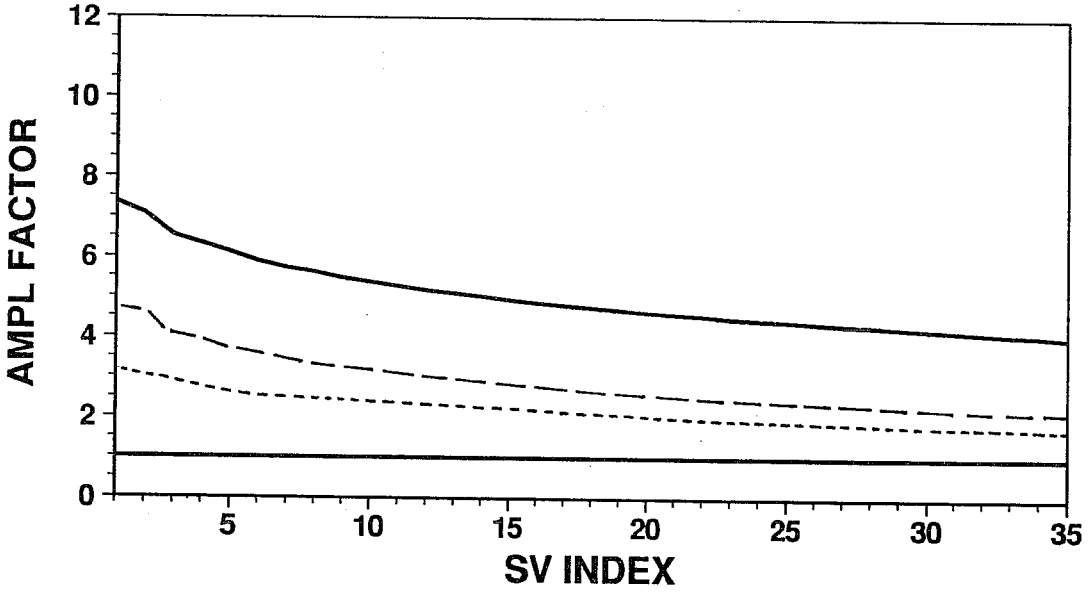

Fig. 4 The mean singular spectrum for the first 35 singular vectors averaged over all winter cases (full line), all spring cases (dashed line), all summer cases (dotted line).

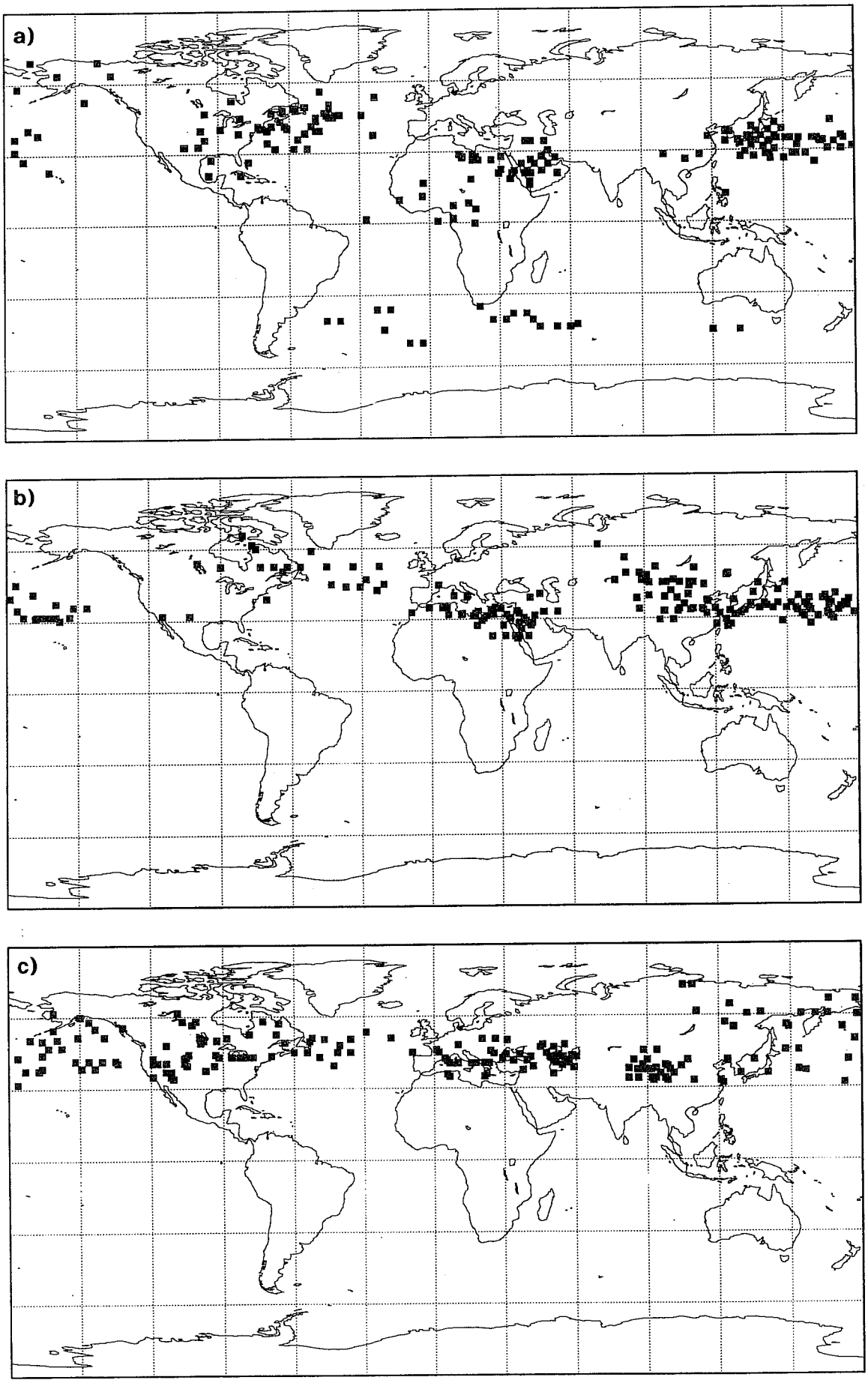

Fig. 5 The distribution of the first 5 singular vectors for a) all winter cases b) all spring cases, c) all summer cases. The position of each singular vector, marked by a square, is determined by its vorticity maximum (at whatever vertical level this occurs).

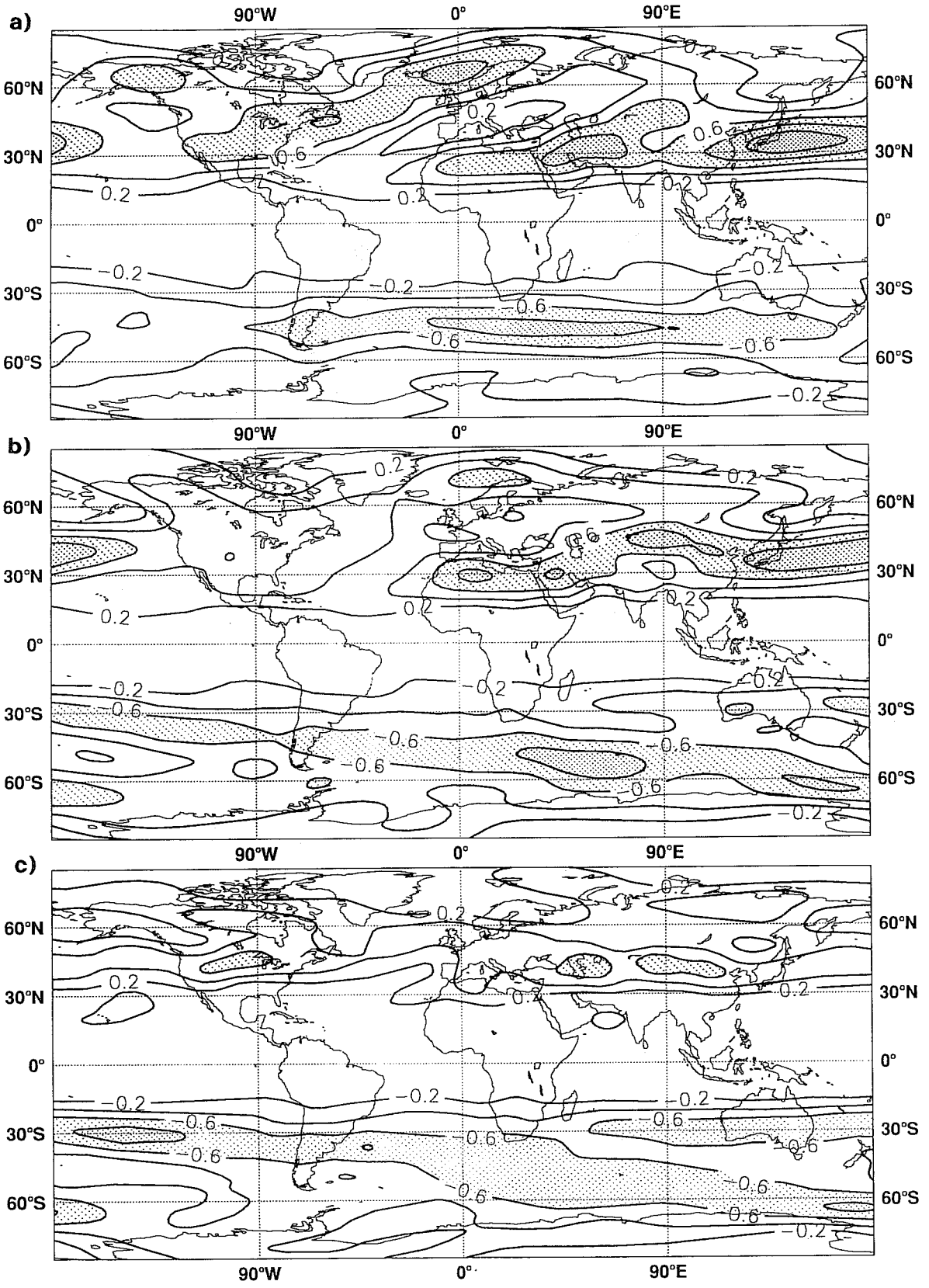

Fig. 6 The distribution of the Eady index, defined by equation (3.1) and using seasonal-mean wind and potential temperature. a) winter 1992/93 b) spring 1993 c) summer 1993. Data from ECMWF operational analyses. Contour interval 0.2/day.

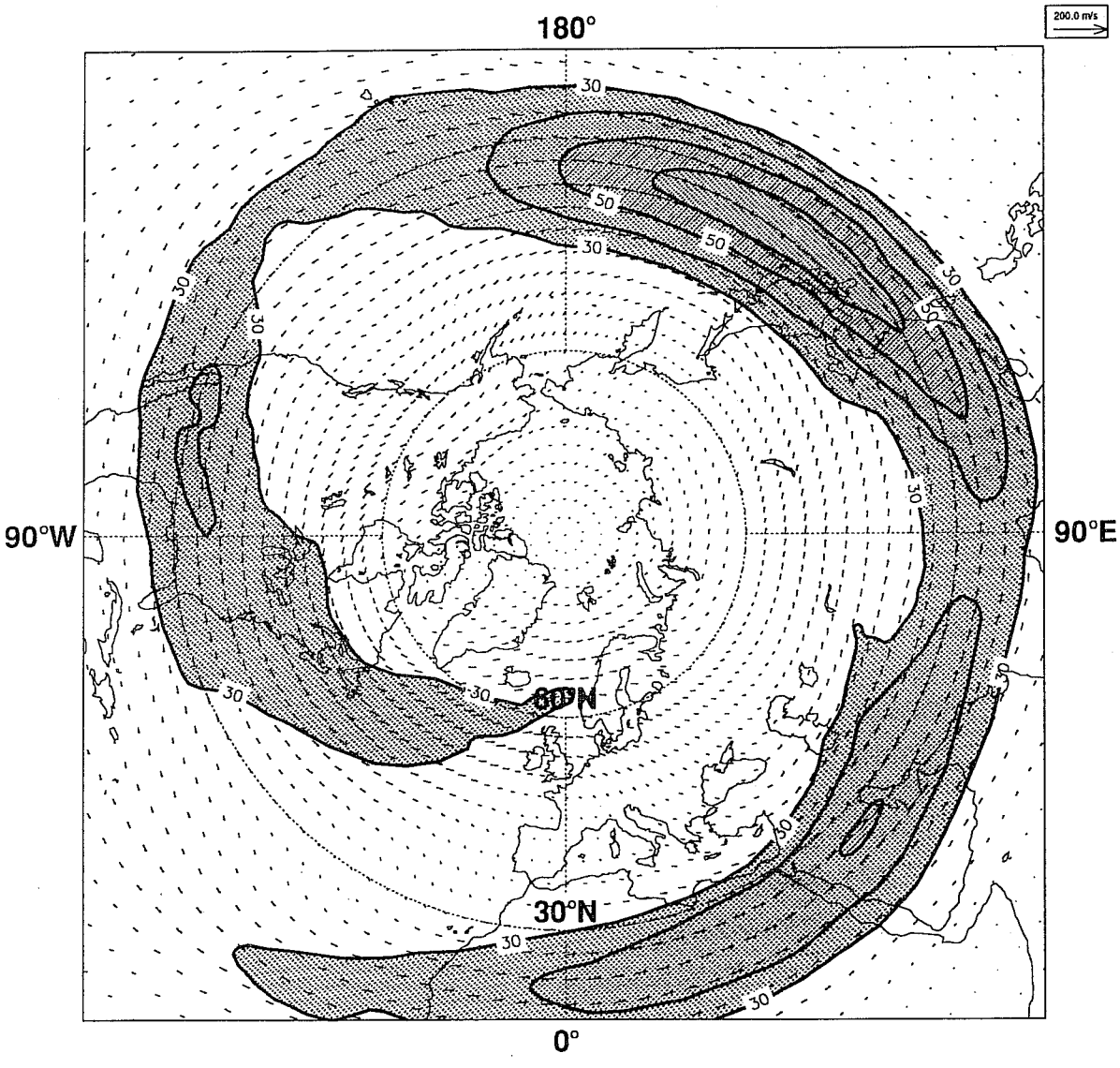

Fig. 7 Seasonal-mean 250 hPa wind vectors and wind speed for winter 1992/93. Data from ECMWF operational analyses.

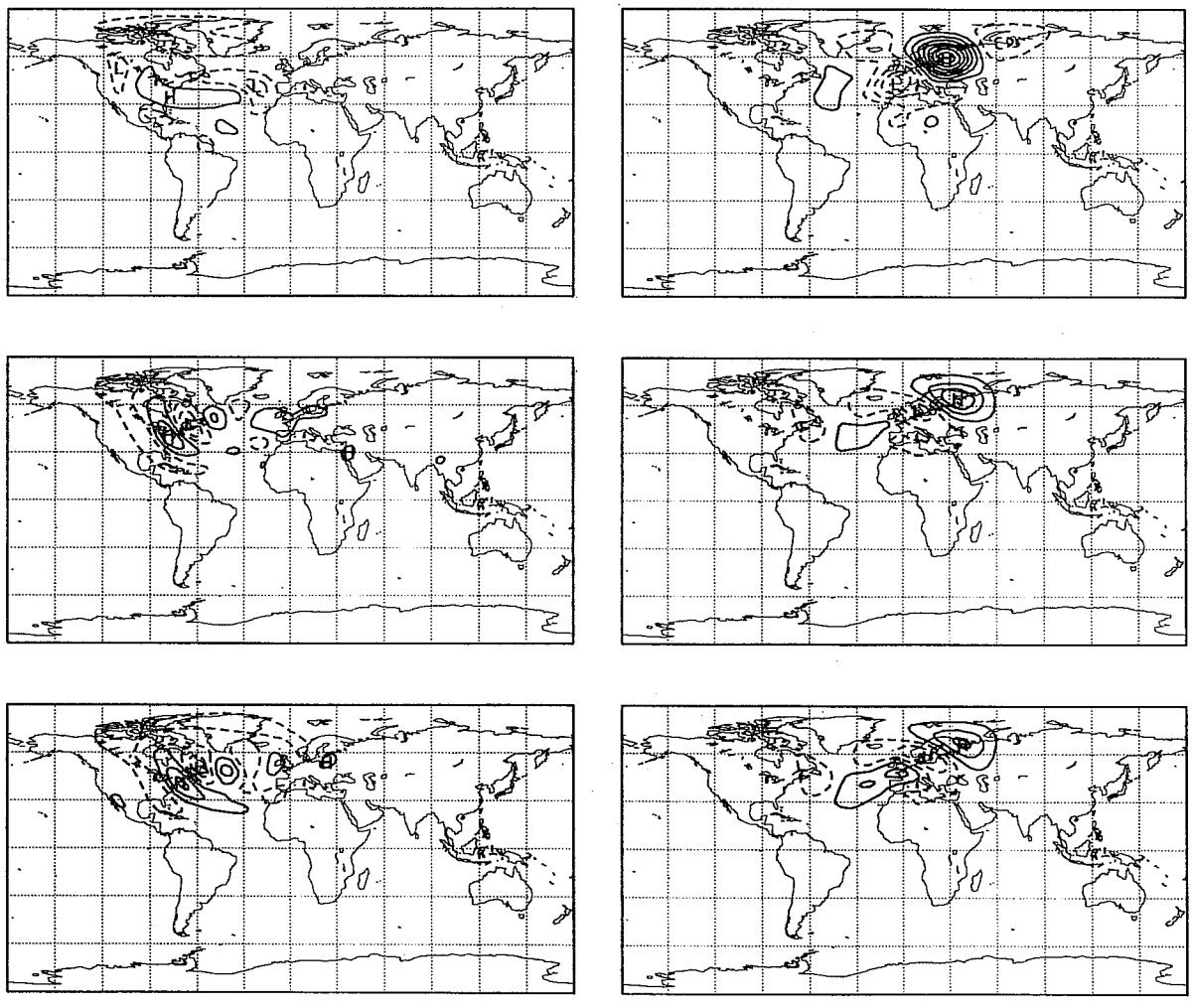

Fig. 8 Streamfunction associated with the dominant singular vector (with 3-day global energy optimization) for 9 January 1993. Left hand panel- initial time. Right hand panel- optimization time. Top row, model level 7 (about 200 hPa). Middle row, model level 13 (about 700 hPa). Bottom row, model level 15 (about 850 hPa). Contour interval at optimization time is 20 times larger than at initial time.

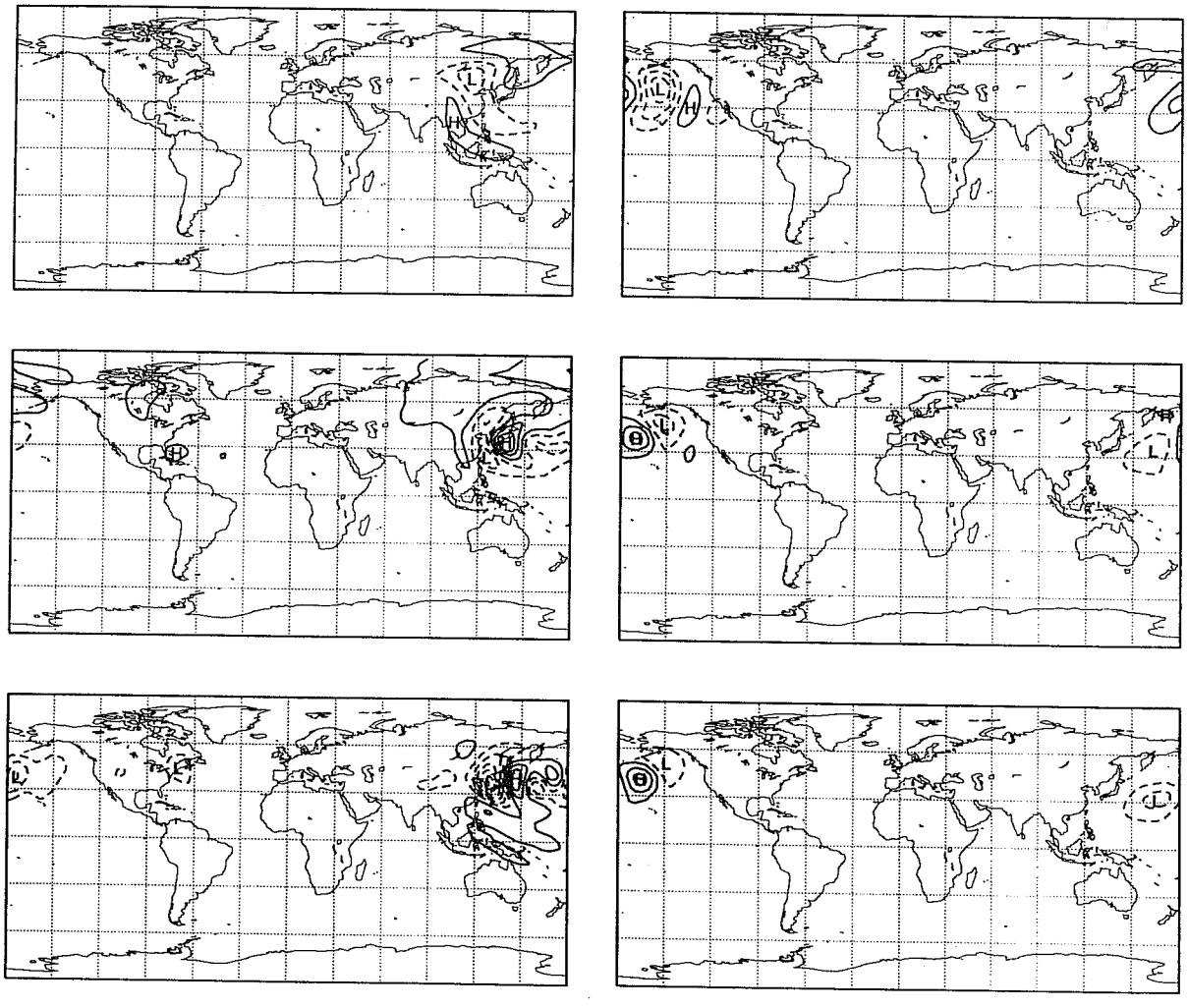

Fig. 9 As Fig. 8 but for 8 February 1993 case.

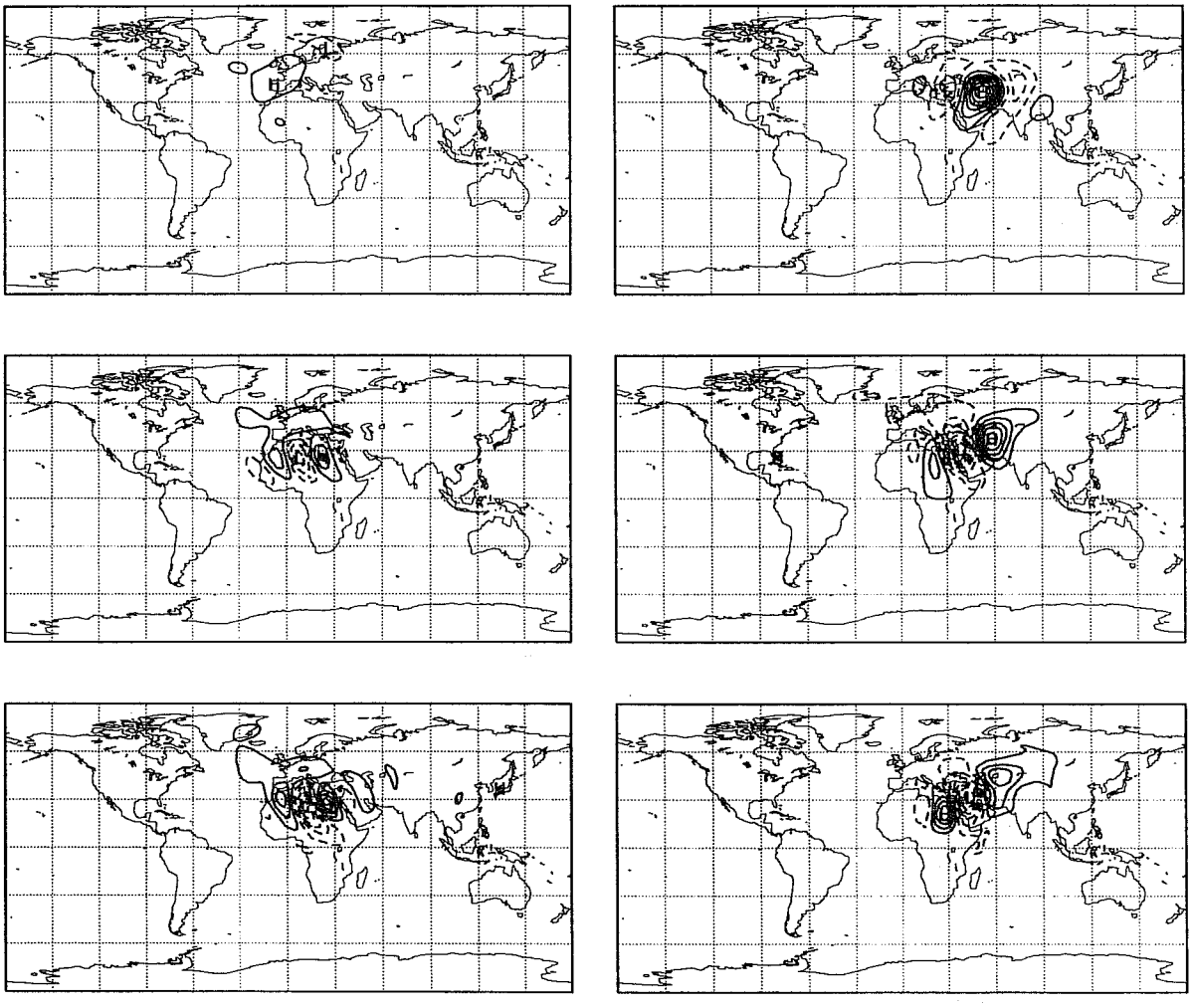

Fig. 10 As Fig. 9 but for 6 March 1993 case.

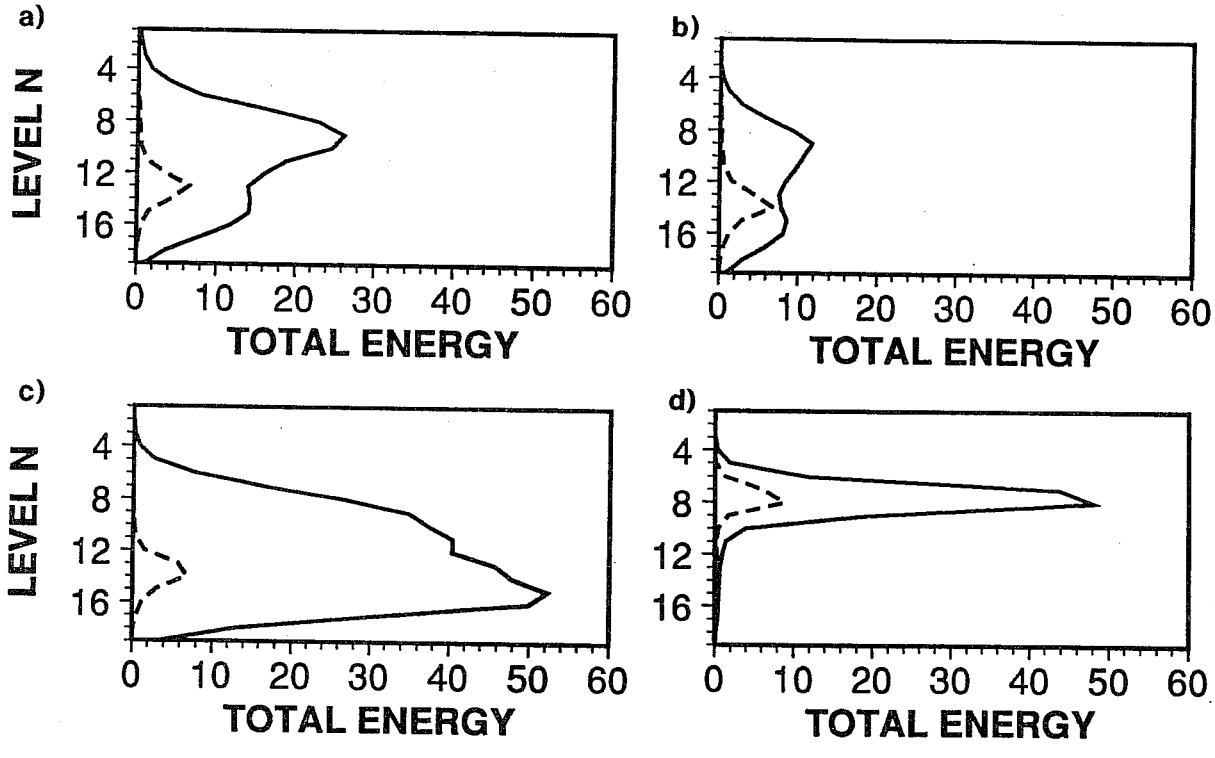

Fig. 11 Total energy of singular vector at initial time (dashed, with values multiplied by a factor of 20 to make them visible on the scale) and optimization time (solid) as a function of model level. a) For 1st singular vector for 9 January case, b) 1st singular vector for 8 February case, c) 1st singular vector for 6 March case d) 4th singular vector for 9 January case.

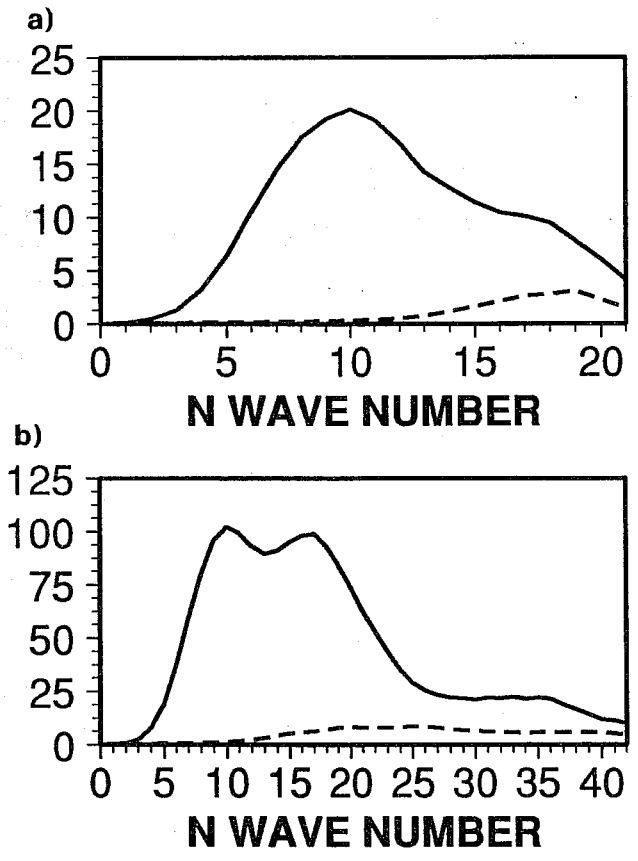

Fig. 12 Energy distribution of singular vector for 9 January case as a function of total wavenumber. Dashed - at initial time (x20). Solid - at optimization time. a) T21 calculation, b) T42 calculation.

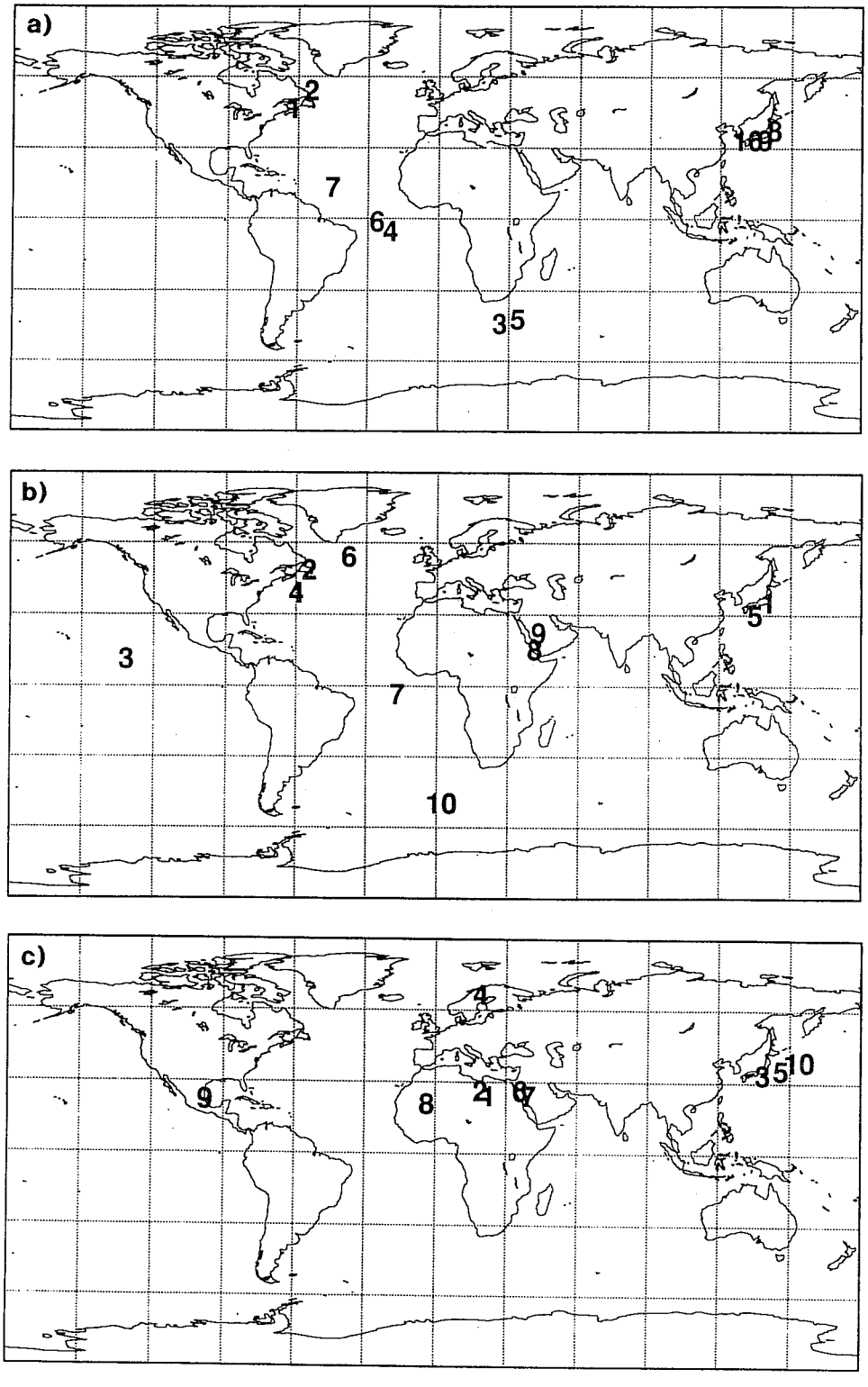

Fig. 13 The position of the vorticity maximum associated with the first 10 singular vectors for a) 9 January case b) 8 February case, c) 6 March case.

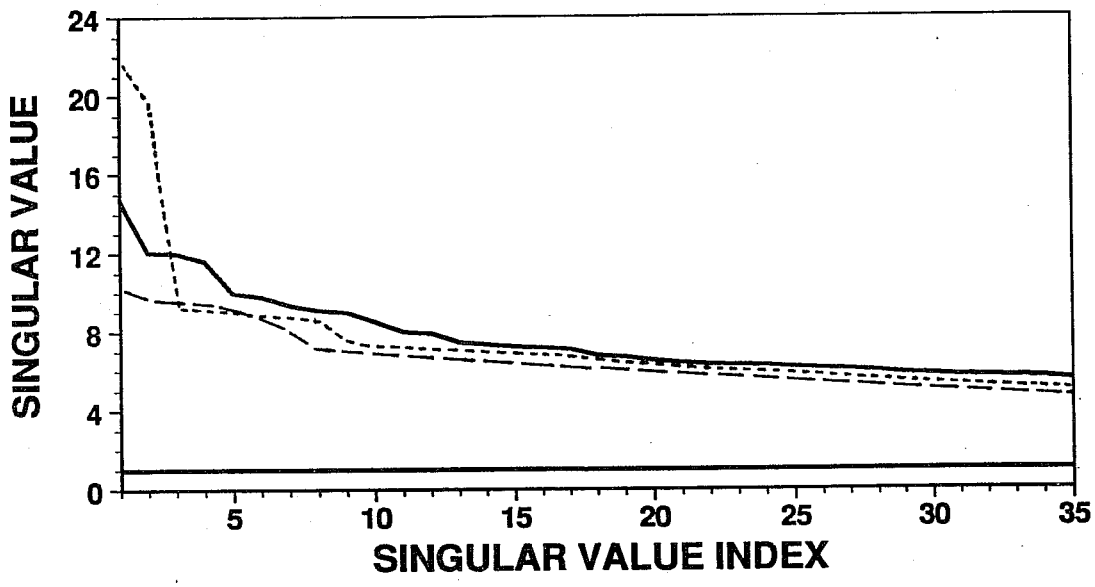

Fig. 14 Spectrum of singular values for 9 January case (solid line), 8 February case (dashed line), 6 March case (dotted line).

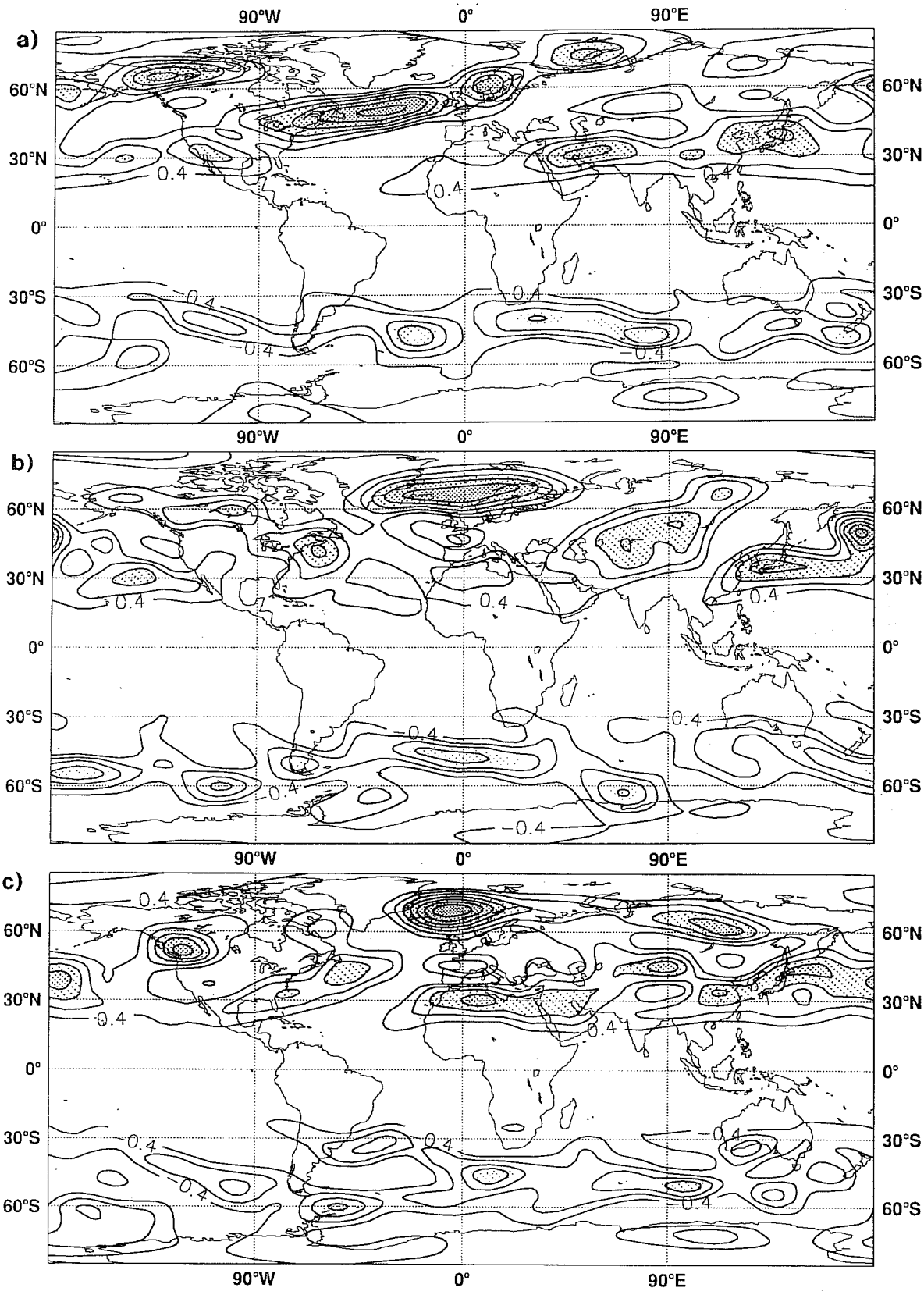

Fig. 15 Eady index for a) 9 January b) 8 February c) 6 March. Contour interval 0.2/day.

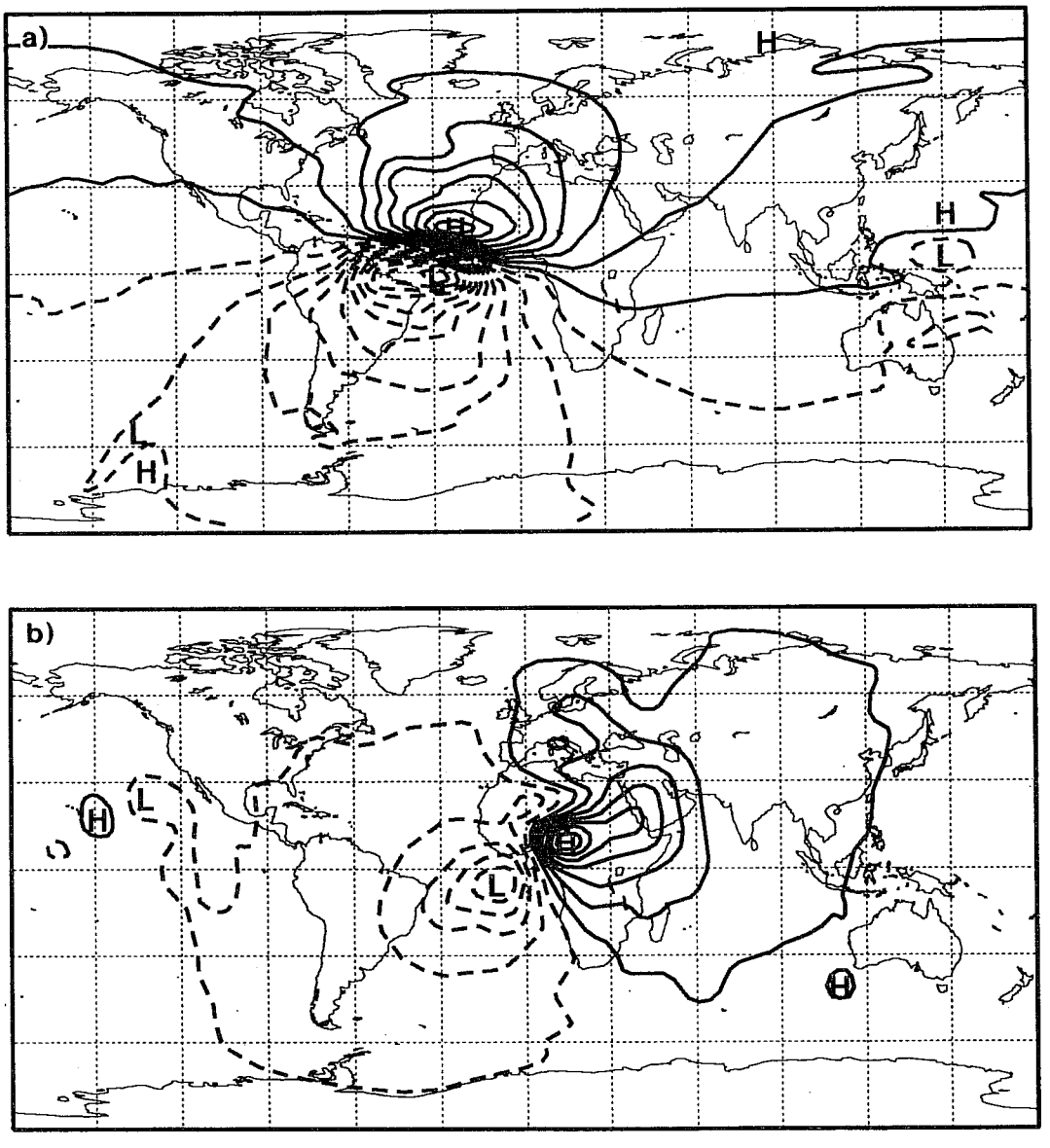

Fig. 16 As Fig. 8 for the 4th singular vector for 9 January (model level 7 only). Top panel initial time. Bottom panel optimization time.

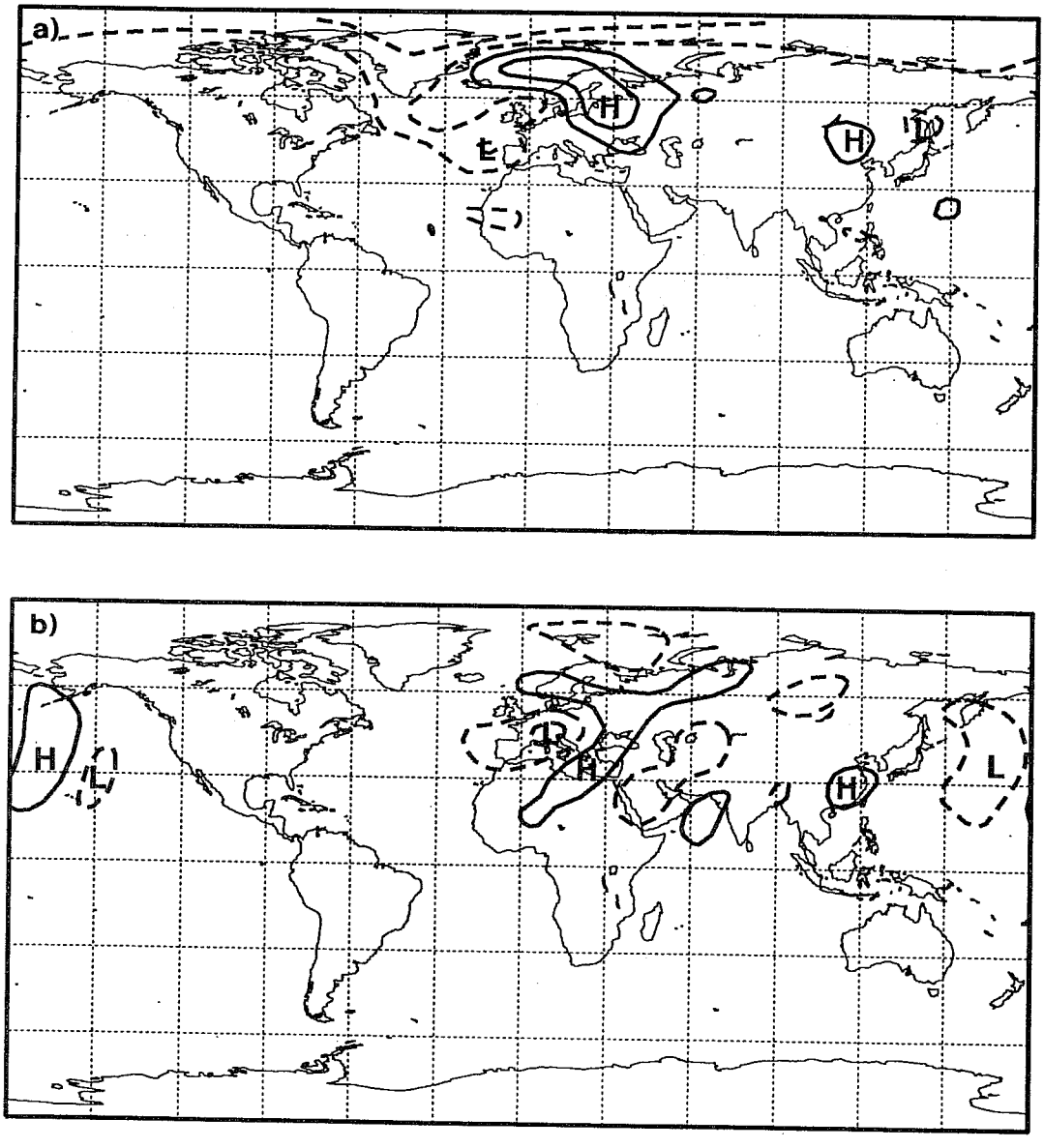

Fig. 17 As Fig. 8 for the 4th singular vector for 6 March (model level 7 only). Top panel initial time. Bottom panel optimization time.

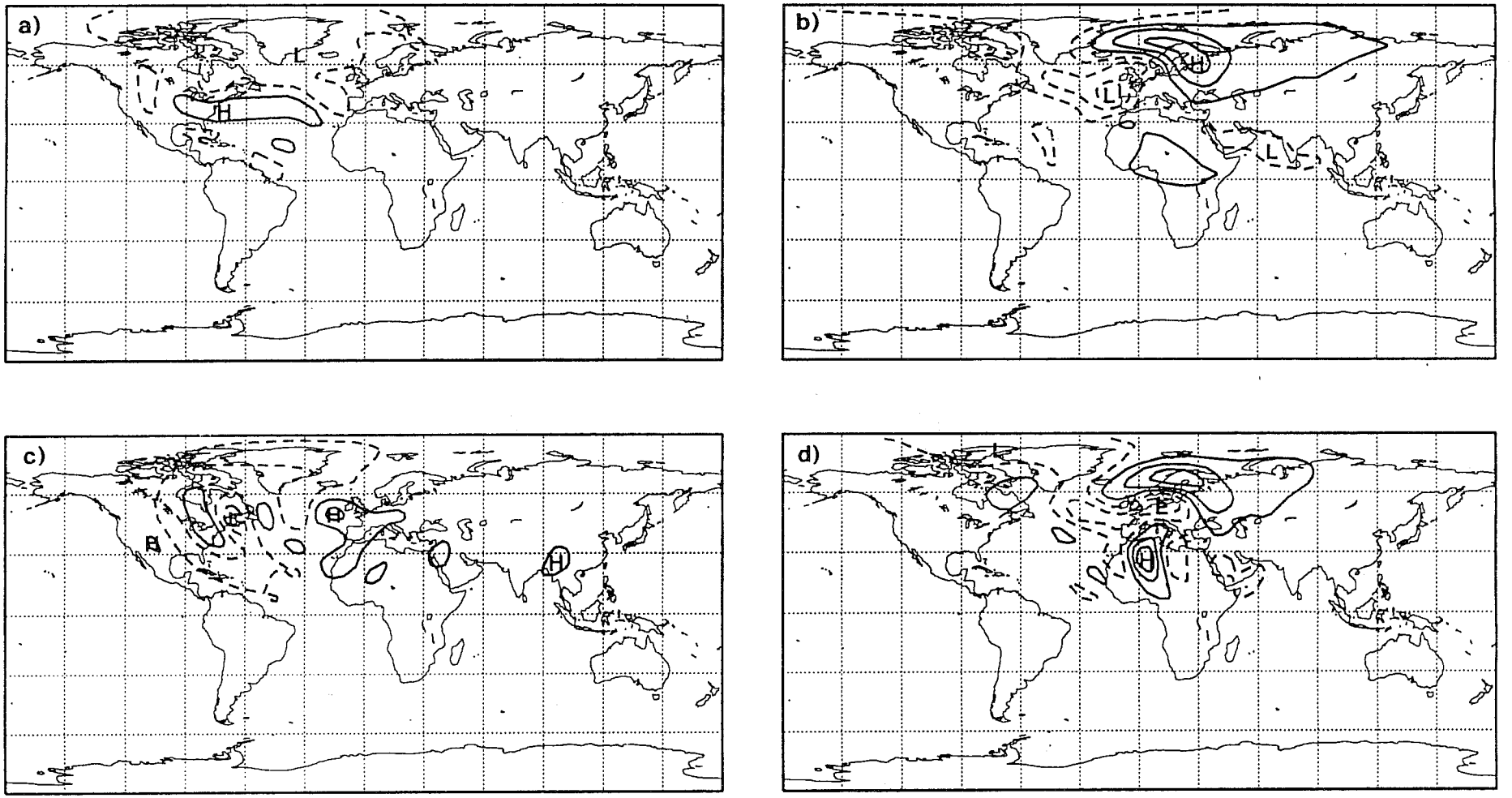

Fig. 18 Streamfunction for the dominant singular vector at initial time (only) with local projection operator applied to target area (30N-60N, 0-30E) for 9 January (left panels), 6 March (right panels). Top row - model level 7 (about 200 hPa). Bottom row - model level 13 (about 700 hPa).

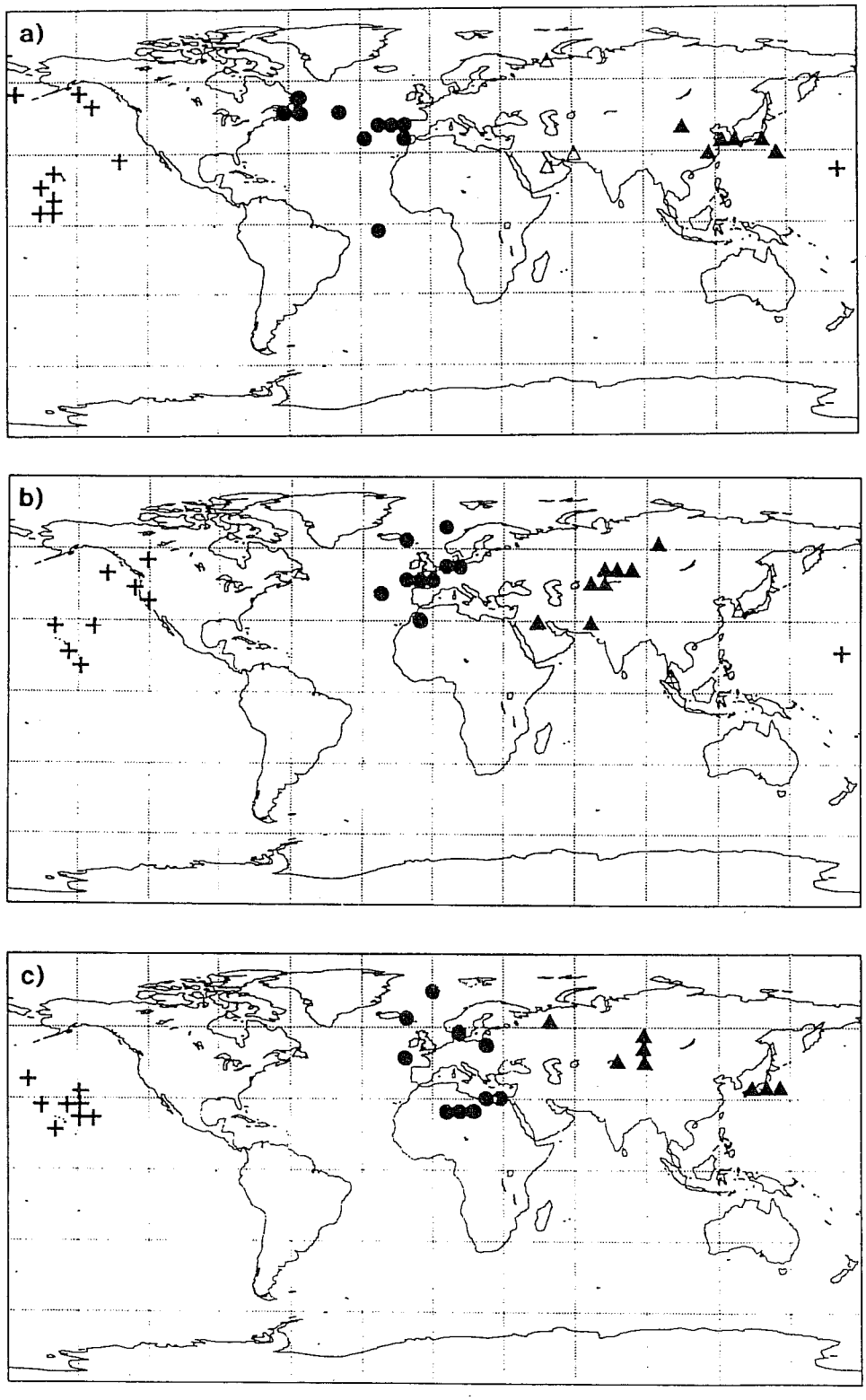

Fig. 19 Position of first 10 singular vectors at initial time, as determined by vorticity maxima, for the three target areas (30N-60N, 0-30E), singular vectors shown as circles; (30N-60N, 120E-150E), singular vectors shown as triangles; (30N-60N, 120W-90W), singular vectors shown as crosses. a) 9 January case, b) 8 February case, c) 6 March case.

TABLE 1

19 December 1992 NA 20 December 1992 P 21 December 1992 P	6 February 1993 A 7 February 1993 A 8 February 1993 P
26 December 1992 P 27 December 1992 28 December 1992 A	13 February 1993 NA 14 February 1993 P 15 February 1993 NA
2 January 1993 NA 3 January 1993 P 4 January 1993 P	20 February 1993 NA 21 February 1993 A 22 February 1993 A
9 January 1993 A 10 January 1993 A 11 January 1993 A	27 February 1993 NA 28 February 1993 NA 1 March 1993 P
16 January 1993 P 17 January 1993 P 18 January 1993 A	6 March 1993 NA 7 March 1993 NA 8 March 1993 NA
23 January 1993 P 24 January 1993 25 January 1993	13 March 1993 A 14 March 1993 A 15 March 1993 A
30 January 1993 A 31 January 1993 A 1 February 1993 A	

Initial dates of singular vectors calculated with the ECMWF operational forecast system. A "P", "A", or "NA" against a date indicates that the dominant singular vector for that date was positioned over the east Asian/ west Pacific, north-east American/ west Atlantic, or north Africa region respectively. Where no symbol is shown against a date, the dominant singular vector was located elsewhere. The position of a singular vector was determined by the its vorticity maximum at initial time.